WetCH4: A Machine Learning-based Upscaling of Methane Fluxes of Northern Wetlands during 2016-2022

Qing Ying[1,2*], Benjamin Poulter[2], Jennifer D. Watts[3], Kyle A. Arndt[3], Anna-Maria Virkkala[3], Brendan M. Rogers[3], Susan M. Natali[3], Lori Bruhwiler[4], Youmi Oh[4,5], Amanda Armstrong[2], Eric J. Ward[1,2], Hilary Sullivan[3], Luke D. Schiferl[6], Clayton D. Elder[7,8], Olli Peltola[9], Annett Bartsch[10], Ankur R. Desai[11], Eugénie Euskirchen[12], Mathias Göckede[13], Bernhard Lehner[14], Mats B. Nilsson[15], Matthias Peichl[15], Oliver Sonnentag[16], Eeva-Stiina Tuittila[17], Torsten Sachs[18,19], Aram Kalhori[18], Masahito Ueyama[20], Zhen Zhang[1,21*]

[1]Earth System Science Interdisciplinary Center, University of Maryland, College Park, MD 20740, USA
[2]Biospheric Sciences Laboratory, NASA Goddard Space Flight Center, Greenbelt, MD 20771, USA
[3]Woodwell Climate Research Center, Falmouth, MA 02540, USA
[4]NOAA ESRL, 325 Broadway, Boulder, Colorado, USA
[5]Cooperative Institute for Research in Environmental Sciences (CIRES), University of Colorado, Boulder, CO 80305, USA
[6]Lamont-Doherty Earth Observatory, Columbia University, Palisades, NY, USA
[7]Jet Propulsion Laboratory, California Institute of Technology, Pasadena, CA, USA
[8]Ames Research Center, Earth Science Division, Moffett Field, CA, USA
[9]Natural Resources Institute Finland (Luke), Latokartanonkaari 9, Helsinki, 00790, Finland
[10]b.geos, Korneuburg, Austria
[11]Department of Atmospheric and Oceanic Sciences, University of Wisconsin, Madison, WI 53706, USA
[12]Institute of Arctic Biology, University of Alaska, Fairbanks, AK 99775, USA
[13]Max Planck Institute for Biogeochemistry, Jena, Germany
[14]Department of Geography, McGill University, Montreal, QC H3A 0B9, Canada
[15]Department of Forest Ecology and Management, Swedish University of Agricultural Sciences, Umeå, Sweden
[16]Département de géographie, Université de Montréal, Montréal, QC, Canada
[17]University of Eastern Finland, School of Forest Sciences, Joensuu, Finland
[18]GFZ German Research Centre for Geosciences, Potsdam, Germany
[19]Institute of Geoecology, Technische Universität Braunschweig, Braunschweig, Germany
[20]Graduate School of Agriculture, Osaka Metropolitan University, Japan
[21]National Tibetan Plateau Data Center (TPDC), State Key Laboratory of Tibetan Plateau Earth System, Environment and Resource (TPESER), Institute of Tibetan Plateau Research, Chinese Academy of Sciences, Beijing, 100101, China

41   *Correspondence to*: Qing Ying (qying@umd.edu) and Zhen Zhang (yuisheng@gmail.com)

Abstract

43   Wetlands are the largest natural source of methane (CH_4) emissions globally. Northern wetlands
44   (>45° N), accounting for 42% of global wetland area, are increasingly vulnerable to carbon loss,
45   especially as CH_4 emissions may accelerate under intensified high-latitude warming. However,
46   the magnitude and spatial patterns of high-latitude CH_4 emissions remain relatively uncertain.
47   Here we present estimates of daily CH_4 fluxes obtained using a new machine learning-based
48   wetland CH_4 upscaling framework (WetCH$_4$) that combines the most complete database of eddy
49   covariance (EC) observations available to date with satellite remote sensing informed
50   observations of environmental conditions at 10-km resolution. The most important predictor
51   variables included near-surface soil temperatures (top 40 cm), vegetation spectral reflectance,
52   and soil moisture. Our results, modeled from 138 site-years across 26 sites, had relatively
53   strong predictive skill with a mean R^2 of 0.51 and 0.70 and a mean absolute error (MAE) of 30
54   nmol m^{-2} s^{-1} and 27 nmol m^{-2} s^{-1} for daily and monthly fluxes, respectively. Based on the model
55   results, we estimated an annual average of 22.8 ±2.4 Tg CH_4 yr^{-1} for the northern wetland
56   region (2016-2022) and total budgets ranged from 15.7 - 51.6 Tg CH_4 yr^{-1}, depending on
57   wetland map extents. Although 88% of the estimated CH_4 budget occurred during the May-
58   October period, a considerable amount (2.6 ±0.3 Tg CH_4) occurred during winter. Regionally,
59   the West Siberian wetlands accounted for a majority (51%) of the interannual variation in
60   domain CH_4 emissions. Overall, our results provide valuable new high spatiotemporal
61   information on the wetland emissions in the high-latitude carbon cycle. However, many key
62   uncertainties remain, including those driven by wetland extent maps and soil moisture products,
63   incomplete spatial and temporal representativeness in the existing CH_4 flux database – e.g.,
64   only 23% of the sites operate outside of summer months and flux towers do not exist or are
65   greatly limited in many wetland regions. These uncertainties will need to be addressed by the
66   science community to remove bottlenecks currently limiting progress in CH_4 detection and
67   monitoring. The dataset can be found at https://doi.org/10.5281/zenodo.10802153 (Ying et al.,
68   2024).

69

70   Keywords
71   Northern high latitudes; wetland; methane (CH_4) flux; eddy covariance; remote sensing;
72   machine learning; data-driven upscaling

1. Introduction

74   Methane (CH_4) is the second most important greenhouse gas after carbon dioxide (CO_2) and
75   has contributed to around 1/3 of anthropogenic warming (IPCC AR6, 2023). Wetlands are the
76   largest natural source of CH_4 emissions. Northern freshwater wetlands (>45° N) account for
77   roughly 40% of global wetland area (ranging 1.3 - 8.7 million km^2; Z. Zhang et al., 2021), yet the
78   amount of CH_4 emissions from this region is highly uncertain – currently estimated to be 22 –
79   49.5 Tg CH_4 yr^{-1} (Aydin et al., 2011; Baray et al., 2021; Heimann, 2011; Kirschke et al., 2013;

80 Peltola et al., 2019; Saunois et al., 2020; Treat et al., 2018; Watts et al., 2023). The
81 uncertainties in the estimates of wetland CH_4 emissions are primarily attributed to challenges in
82 mapping vegetated wetlands versus open water leading to double counting (Thornton et al.,
83 2016), seasonal wetland dynamics and uncertainties in estimates on flux rates.
84
85 Characterized by nutrient, moisture and hydrodynamic conditions, northern freshwater wetlands
86 are classified as wet tundra in treeless permafrost areas, peat-forming bogs and fens in boreal
87 and temperate biomes, and permafrost bogs (Olefeldt et al., 2021; Kuhn et al., 2021). Bogs
88 were estimated to cover the largest area (1.38-2.41 million km^2) in the northern high latitudes,
89 followed by fens (0.76-1.14 million km^2) and wet tundra (0.31-0.53 million km^2) (Olefeldt et al.
90 2021). Climate change poses significant threats to these wetlands, affecting their extent and the
91 duration of conditions suitable for wetland formation in permafrost zones (Avis et al., 2011). The
92 rates of CH_4 emissions may increase quickly because of intensified warming at the northern
93 high latitudes (Masson-Delmotte et al., 2021; Rawlins et al., 2010; Rößger et al., 2022; Walsh,
94 2014; Z. Zhang, Poulter, et al., 2023).
95
96 Reflecting CH4 response to warming, northern wetlands may account for a high portion
97 (~78.5%) of the global surface emissions anomaly of CH_4 in 2020 relative to 2019 (6.0 ± 2.3 Tg
98 CH_4 yr^{-1}) (S. Peng et al., 2022; Z. Zhang, Poulter, et al., 2023). This is concerning as the
99 responses of high latitude CH_4 emissions to a warming and possibly wetting climate could
100 produce a positive carbon-climate feedback (McGuire et al., 2009; Natali et al., 2019).
101 However, the ability of models to account for and predict the spatio-temporal variability of high
102 latitude wetland CH_4 emission rates remain very limited (Treat et al., 2024).
103
104 Field observations of gas fluxes typically measure CH_4 exchange between the land and
105 atmosphere at sub-meter to ecosystem (100s of m to km) scales (Bansal et al., 2023; Chu et al.,
106 2021). Tower eddy covariance (EC) methods provide near-continuous measurements over
107 ecosystem-scale footprints (5 – 100 x 10^3 m^2), the size of which matches fine to medium
108 resolution satellite remote sensing. Typical EC measurement system records include carbon,
109 water and energy fluxes along with environmental conditions at half-hourly intervals. Long-term
110 EC datasets can support the analysis of daily, monthly, seasonal, or interannual patterns and
111 drivers of carbon fluxes (Baldocchi, 2003). Chambers can also measure CH_4 fluxes, though at
112 sub-meter resolution and small spatial coverage area (Kuhn et al., 2021; Bansal et al., 2023).
113 Most chamber studies have a limited temporal sampling period. To avoid footprint disagreement
114 between EC and chamber measurement techniques, we focused on EC-based CH_4 upscaling in
115 this study.
116
117 Data-driven upscaling uses empirical models (Bodesheim et al., 2018; Jung et al., 2011),
118 including machine learning (ML) approaches, to compute CH_4 fluxes. It provides independent
119 estimates to those from process-based models and atmospheric inversions (Bergamaschi et al.,
120 2013; Spahni et al., 2011). These approaches have been used to estimate CH_4 fluxes from
121 various ecosystems such as northern wetlands (Peltola et al., 2019; Virkkala et al., 2023; Yuan
122 et al., 2024), global reservoirs (Johnson et al., 2021), and global aquatic ecosystems
123 (Rosentreter et al., 2021).

124
125 Two types of methods are generally used for data-driven upscaling. The first uses a look-up
126 table approach and applies emission rates or emission factors via data synthesis to the
127 corresponding land surface areas, or activity data, over the study region. Emission rates from
128 field observations are associated with environmental drivers that have been spatially
129 characterized and are then applied to the land covers with the same environmental drivers. For
130 example, Rosentreter et al. (2021) collected 2,601 CH_4 flux records measured using various
131 methods through a literature review and characterized emission rates over 15 aquatic
132 ecosystem types to upscale global aquatic CH_4 emissions. The study provided estimates of total
133 and per ecosystem emissions but did not produce spatial distributions and was unable to
134 estimate temporal changes. A similar method was applied for the northern permafrost region,
135 where statistical CH_4 flux rates from the Boreal-Arctic Wetland and Lake CH_4 Dataset (BAWLD-
136 CH_4) were analyzed for emission estimation by wetland type (Kuhn et al., 2021; Ramage et al.,
137 2024). This method favors homogeneous ecosystems and static environments, and the results
138 may be biased for large-scale studies where spatial heterogeneity is prevalent.
139
140 Another approach uses ML methods to upscale fluxes (Bodesheim et al., 2018; Tramontana et
141 al., 2016; Yuan et al., 2024). ML models are developed with large training datasets. Generally,
142 ML models can learn from high-dimensional data by optimizing many statistical parameters and
143 identifying variables that are closely associated with spatio-temporally varied CH_4 emissions.
144 The efficient computation cost makes it easier to apply the models over large regions at higher
145 spatial resolutions. Among ML methods, decision-tree-based algorithms have been widely used
146 in upscaling for computation efficiency and prediction performance (Beaulieu et al., 2020; Jung
147 et al., 2020; Virkkala et al., 2021; C. Zhang et al., 2020). Specifically, Random Forests (RF)
148 were utilized in regional to global wetland CH_4 upscaling (Davidson et al., 2017; Feron et al.,
149 2024; McNicol et al., 2023; Peltola et al., 2019) for the robustness and prevention of overfitting
150 to noise in the input data. For example, Peltola et al. (2019) used RF and EC measurements to
151 upscale monthly CH_4 fluxes from the northern wetlands at 0.25°- 0.5° spatial resolution over the
152 2013-2014 period.
153
154 ML-based upscaling studies usually incorporate information from remote sensing to inform
155 wetland extent, changes in vegetation and other surface biophysical properties (Davidson et al.,
156 2017; Virkkala et al., 2023; Watts et al., 2014, 2023). For example, recent ML-based large-scale
157 upscaling approaches used MODIS land surface temperature at night (LST), enhanced
158 vegetation index (EVI), vegetation canopy height, and ancillary environmental variables from
159 remote sensing products (McNicol et al., 2023; Ouyang et al., 2023; Peltola et al., 2019) (See
160 Supporting Materials Text 1 and Table S1 for detailed predicting variables used in existing ML-
161 based wetland CH_4 upscaling products). However, soil moisture and soil temperature, two
162 controlling factors of wetland CH_4 fluxes (Knox et al., 2021; Yuan et al., 2022), were missing in
163 previous ML-based regional to global upscaling studies. Soil moisture has been identified as
164 one of the important controlling factors for freshwater wetland CH_4 fluxes (Euskirchen et al.,
165 2024; Voigt et al., 2023). This is the first ML-based study that incorporates remote sensing
166 constraints from Soil Moisture Active Passive (SMAP) microwave-sensed soil moisture and
167 Moderate Resolution Imaging Spectroradiometer Nadir Bidirectional Reflectance Distribution

168   Function (BRDF) – Adjusted Reflectance (MODIS NBAR) data. Surface reflectance provides
169   information of vegetation properties that affect the production and transport of CH_4 to the
170   atmosphere, and ecosystem wetness (Alonso et al., 2020; Chen et al., 2013; Houborg et al.,
171   2007; Murray-Hudson et al., 2015; Z. Wang et al., 2018; Entekhabi et al., 2010).
172
173   The goal of this study is to develop a scalable framework to upscale daily CH_4 fluxes from EC
174   observations to northern latitude wetlands (>45° N) using the ensemble RF ML approach with a
175   suite of reanalysis and remote sensing products representing spatiotemporal environmental
176   conditions. Our specific objectives are to:
177   1. compile an updated EC-based CH_4 flux dataset that extends the temporal and spatial
178   coverage of the Fluxnet-CH_4 database (Delwiche et al., 2021) for the northern high
179   latitudes.
180   2. build ensemble RF models of CH_4 fluxes at site-level based on *in-situ* measured
181   variables and then at grid-level using gridded reanalysis inputs and constraints from
182   satellite remote sensing.
183   3. apply grid-level models to produce a 10-km gridded daily distribution of CH_4 flux product
184   for the northern high latitudes' wetlands using bootstrapped models and their derived
185   uncertainties (Table S1).

2. Materials and methods

2.1 Overview

188   The scalable framework of upscaling CH_4 fluxes from EC observations for wetlands (referred to
189   as WetCH4 hereafter), which selects predictors at the site level and constructs upscaling models
190   at a grid level, is illustrated in Fig. 1. *In situ*, reanalysis, and remote-sensing products were
191   compiled as candidate predictors for modeling (Fig. 1, purple boxes; see section 2.2 for details).
192   We first ran a feature selection, which uses ensemble RF models to choose important predictors
193   from an extensive list of *in situ* variables available from the flux tower sites. Gridded versions of
194   selected site variables were taken from Modern-Era Retrospective analysis for Research and
195   Applications (MERRA2) reanalysis (Gelaro et al., 2017) to model with RF at grid level. We then
196   added remote sensing-based products from MODIS NBAR and SMAP soil wetness, as well as
197   topographic data, to strengthen the model and provide finer delineation of environment
198   gradients based on literature and expert knowledge. The predictive performance of grid-level
199   models with input variables at their native spatial resolution (except for MERRA2 that were
200   interpolated to 10-km resolution) was then evaluated. We also compared model performance
201   with those from two additional ML algorithms: support vector machines (SVM) and artificial
202   neural network (ANN) (Fig. 1 pink boxes). The ML algorithm with the highest mean R^2 and
203   lowest daily mean errors in model predictive performance was selected for bootstrap modeling
204   and upscaling the 0.098° (~10km along latitudinal length) gridded time series of daily CH_4 fluxes
205   and ensemble uncertainty estimation (Fig. 1 grey boxes).
206

207
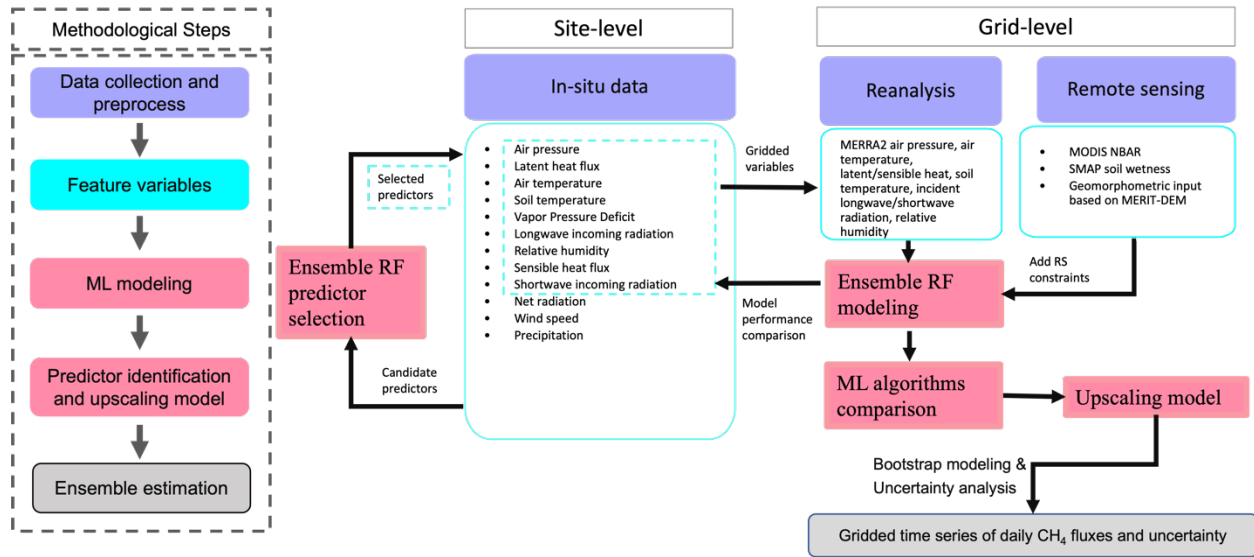
208 Fig. 1 Workflow and experimental design: abstract methodological steps are integrated in the
209 dashed box on the left, while a detailed experimental design is described on the right. Colors on
210 the right match the associated step on the left.
211
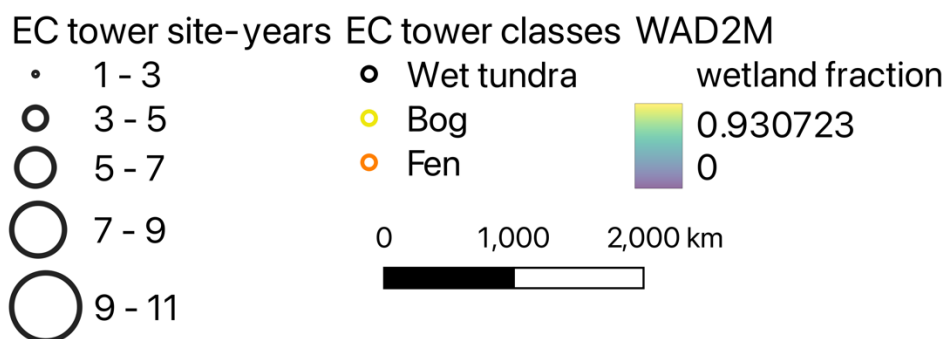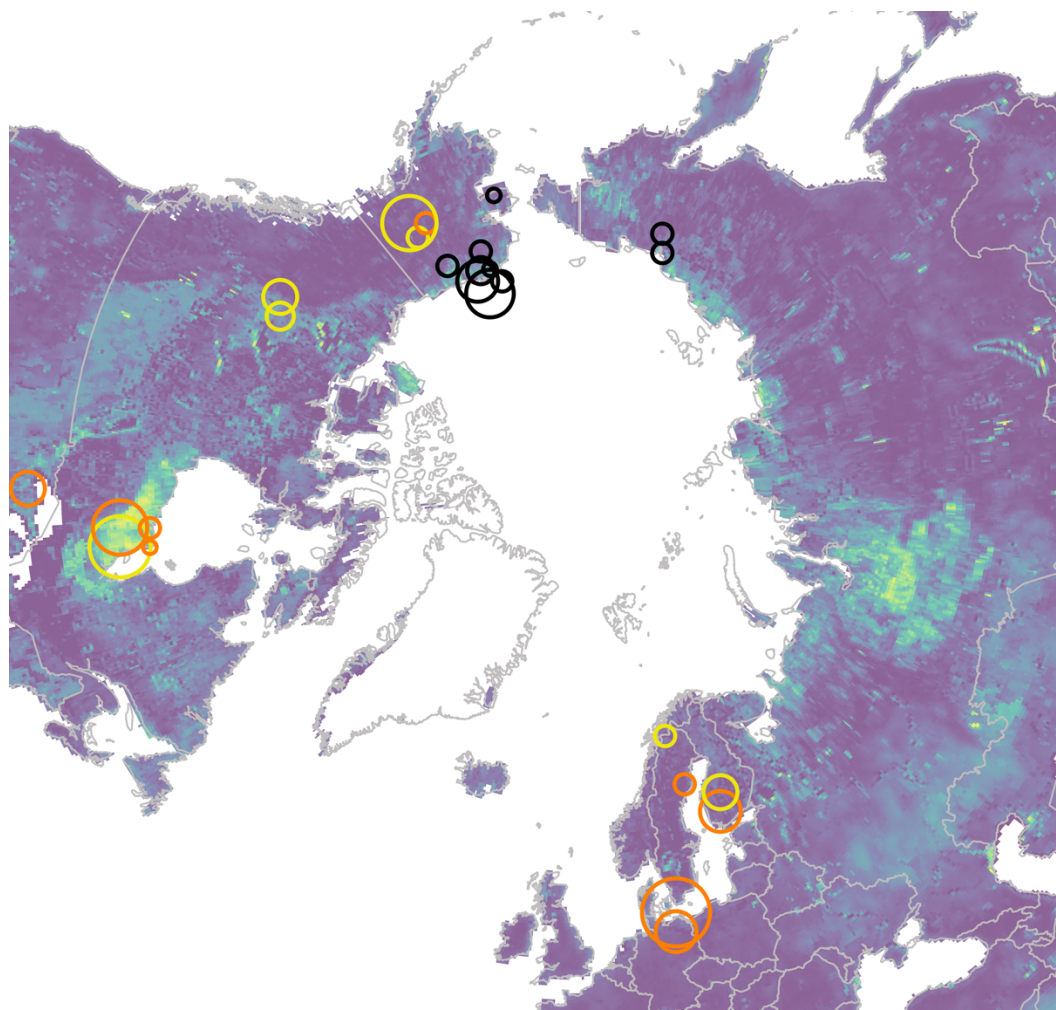
212
213 Fig. 2 Eddy covariance tower sites: distribution (>45° N), class, and data size (site-years) used
214 in WetCH$_4$. Colored circles represent EC tower locations and land cover classes, with wetland
215 sites in cyan (wet tundra), yellow (bog) and orange (fen). The circle sizes represent observation
216 years(n) of available CH$_4$ fluxes at the site (e.g. 1-3 stands for 1<=n<3). The background image
217 shows the estimated maximum annual fractions of wetland cover in 2011-2020 from WAD2M (Z.
218 Zhang et al., 2021).

2.2 Data

2.2.1 Eddy covariance measurements

The base of our EC data collection stems from a publicly available global synthesis coordination of FLUXNET-CH_4 (Delwiche et al., 2021; Knox et al., 2019), which includes 79 EC tower sites (42 are freshwater wetland sites) and 293 site-years of data. Fluxnet-CH_4 represents a first compilation of global CH_4 fluxes measured by EC towers (Delwiche et al., 2021; Knox et al., 2019), yet more EC data exists outside of the network. We collected both daily and half-hourly data from 44 sites in the northern high latitudes (>45° N), accounting for 167 site years as our base dataset, to which we added data from 6 new sites (31 site-years) and added additional data to 9 existing sites (21 site-years) contributed by principal investigators (Table S2). In total, we assembled data from 50 EC tower sites in northern latitudes (219 site-years), of which 33 are from wetlands (155 site-years), with 13 wet tundra sites, 11 fens, and 9 bogs. Data entries with missing data in gridded predictors were excluded, including 5 wetland sites (FI-LOM, DE-SFN, RU-SAM, RU-VRK, SE-ST1) where data was collected before SMAP data was available. Another 2 sites (CA-BOU, RU-COK) were excluded after quality control as described further down. As a result, daily and half-hourly EC data from the 26 wetland sites were compiled for analysis from 22 sites in FLUXNET-CH_4 (among which 8 sites with updated data to recent years including US-ATQ, US-BEO, US-BES, US-BRW, US-IVO, US-NGB, US-NGC, US-UAF) and 4 additional sites using information provided directly by principal investigators (including CA-ARB, CA-ARF, CA-PB1, CA-PB2), consisting of 138 site-years data in total and representing the largest high latitude EC-data compilation for CH_4 to date (Table S2, see Supporting Materials Text 2). The sites were distributed among wetland types, including 9 fens, 7 bogs, and 10 wet tundra sites (Fig. 2). RU-CHE and RU-CH2 were two Chersky sites in East Siberian Russia about 600m apart from each other to form a paired disturbance experiment. RU-CH2 was a control tower over an undisturbed wetland, whereas RU-CHE was a tower affected by artificial drainage. The above-ground conditions of the two sites were virtually identical, but soil temperature and moisture were different. Drainage caused lower CH_4 fluxes at RU-CHE compared to those at RU-CH2. However, the SMAP data could not discern the drainage impact on soil moisture at the RU-CHE site due to a coarser spatial resolution, thus it was excluded from grid-level modeling.

Half-hourly fluxes acquired from FLUXNET-CH_4 were already gap-filled (see Supporting Materials Text 2; Irvin et al., 2021). Additional half-hourly fluxes acquired from site PIs were not gap-filled, and as such we performed per site gap filling following the FLUXNET-CH_4 approach (Irvin et al., 2021; Knox et al., 2019). Gap-filled fluxes were temporally consistent and agreed with validation data (mean R^2 = 0.68 and mean RMSE = 6 nmol m^{-2} s^{-1}, *see* Supporting Materials Text 2).

The mean difference in daily mean fluxes between the gap-filled data and the original data converged to -0.2 nmol m^{-2} s^{-1} when there were more than 11 half-hourly EC tower observations in a day but showed substantial bias and larger differences when including days with less than 11 half-hourly observations (Fig. S1). Therefore, daily data entries were only kept when the

261 number of half-hourly EC tower observations per day was greater than 11. All data were
262 retained on four sites where only daily, quality-filtered, data were provided by site PIs (Table
263 S2). As a result, we identified 12,784 daily data entries for upscaling models (Table
264 S2), spanning 2015-2021 with seasonal observation distributions of 44.0% in June-July-August
265 (JJA), 29.0% in March-April-May (MAM), 24.5% in September-October-November (SON), and
266 2.5% in December-January-February (DJF) (Fig. S2).
267
268 Site-level candidate predictors were identified by their known influences on CH_4 fluxes at multi-
269 day to seasonal scales from field control experiments, *in situ* flux synthesis, and process-based
270 modeling (Bloom et al., 2010, 2017; Knox et al., 2021; Olefeldt et al., 2013, 2017). *In situ*
271 candidate predictors that were gap-filled and available in FLUXNET-CH_4 included daily
272 averages of air temperature, soil temperature, air pressure, vapor pressure deficit, relative
273 humidity, latent heat flux, sensible heat flux, longwave incoming radiation, shortwave incoming
274 radiation, net radiation, wind speed, and daily total precipitation (Fig. 1 site-level model solid
275 blue box). We were unable to include water-table depth (WTD) or soil water content (SWC) in
276 our site-level model as they were not available at many sites. However, we explored ML results
277 that included WTD or SWC for a subset of individual sites (36% of total) where these variables
278 were available (see Supporting Materials Text 2 for more details).
279

280 ## 2.2.2 Reanalysis data and satellite data products

281 Reanalysis data were used as the gridded input to replace selected predictors at the site level
282 for training the grid-level models and upscaling. These data provided long-term continuous
283 estimates of nearly all the candidate predictors of the *in situ* measured variables (Fig. 1).
284 MERRA2 is an atmospheric reanalysis of the modern satellite era produced by NASA's Global
285 Modeling and Assimilation Office (Gelaro et al., 2017). We calculated daily means for air
286 pressure, surface air temperature, latent heat flux, sensible heat flux, downward-incoming
287 shortwave radiation, downward-incoming longwave radiation, and soil temperature at three
288 depths (9.88 cm, 19.52 cm, 38.59 cm) (Jiao et al., 2023), and relative humidity using the hourly
289 average of surface flux diagnostics, land surface diagnostics, and land surface forcings. The
290 original 0.5° x 0.625° resolution data were resampled to 0.5° grids using a bilinear interpolation
291 method in the NASA MERRA2 web service tool available on GES DISC. The MERRA2 data
292 were further bilinearly interpolated from 0.5° to 0.098° grids weighted by the multiple-error-
293 removed improved-terrain digital elevation model (MERIT-DEM) at 90-m resolution that
294 significantly improves elevation estimates in flat terrain over previous DEM products (Yamazaki
295 et al., 2017). Daily time series of the nearest 0.098° grid to each EC location were extracted for
296 grid-level modeling, whereas daily grids were input for the 10-km upscaling products.
297

298 To improve the predictive performance of grid-level models, we added remotely sensed
299 biophysical variables, including SMAP soil wetness, MODIS NBAR bands, and topographic data
300 (Fig. 1, Table 1). All remote-sensing products were extracted in daily time steps and their native
301 spatial resolutions at EC tower sites for modeling and aggregated to 0.098° grids over the study
302 domain for upscaling using Google Earth Engine. We filtered out data gaps in SMAP and
303 MODIS NBAR time series extracted at the native spatial resolution during model training and

validation. Gaps in MODIS NBAR were negligible when aggregated from 500-m to 0.098° grids. Gaps in winter SMAP data were filled with zero values to represent frozen soils for upscaling.

The SMAP soil moisture product is generated using passive microwave radiometer-measured brightness temperature merged with estimates from the GEOS Catchment Land Surface and Microwave Radiative Transfer Model in a soil moisture data assimilation system, providing global products of surface and rootzone soil moisture (Reichle et al., 2017). For soil moisture, we employed Level 4 daily soil wetness products (SPL4SMGP.007) from the SMAP mission as proxies for water-table depth in the grid-level model (Reichle et al., 2017). Surface, rootzone, and soil profile wetness are dimensionless variables that indicate relative saturation for top layer soil (0-5 cm), root zone soil (0-100 cm), and total profile soil (0 cm to model bedrock depth), respectively. These three variables are originally 3-hourly data at 9-km resolution and were converted to daily means.

Static topographic variables were added as additional attributes in the grid-level model. We used topographical slope and indices that represent the water flow from MERIT-DEM based on Geomorpho90m (Amatulli et al., 2020). Two topographic indices were applied: the compound topographic index (cti) is considered a proxy of the long-term soil moisture availability, and the stream power index (spi, https://gee-community-catalog.org/projects/geomorpho90/) reflects the erosive power of the flow and the tendency of gravitational forces to move water downstream. We tested the impact of elevation on model performance in explaining inter-site variability of CH_4 upon the current locations of wetland EC sites (see Supporting Materials Text 6). Nevertheless, elevation was not considered an ecologically controlling factor for wetland CH_4 fluxes, and hence was excluded from the input variable importance analysis that ranked the importance of predictors to the prediction accuracy in RF models.

We included MODIS NBAR (MCD43A4v061) products as predictor variables to represent the vegetation layer in the grid-level model in order to enhance our model predictive performance in vegetated wetlands. The 7 NBAR bands (including red/green/blue, 2 near infrared, and 2 shortwave infrared) are developed daily at 500-m spatial resolution, using 16 days of Terra and Aqua data to remove view angle effects, and it is temporally weighted to the ninth day as the best local solar noon reflectance (Schaaf et al., 2002; Z. Wang et al., 2018). We did not explicitly include a vegetation productivity variable, because such information is retained in MODIS NBAR that is used to produce vegetation indices. Emergent aerenchymous vegetation is another important component in the plant-mediated pathway of CH_4 transport yet was less represented in existing upscaling models (Table S1).

Table 1. Description of input variables for grid-level upscaling model

Variable type	Name	Description	Unit	Data source	Native/Model Spatial resolution	Native Temporal resolution
Reanalysis	tas	surface air temperature	°C	MERRA2	0.625°×0.5°/10km	1 hourly

Reanalysis	pa	surface air pressure	Kpa	MERRA2	0.625°×0.5°/10km	1 hourly
Reanalysis	le	latent heat	W m^{-2}	MERRA2	0.625°×0.5°/10km	1 hourly
Reanalysis	h	sensible heat	W m^{-2}	MERRA2	0.625°×0.5°/10km	1 hourly
Reanalysis	rsdl	downward-incoming longwave radiation	W m^{-2}	MERRA2	0.625°×0.5°/10km	1 hourly
Reanalysis	rsds	downward-incoming shortwave radiation	W m^{-2}	MERRA2	0.625°×0.5°/10km	1 hourly
Reanalysis	spfh	surface specific humidity	unitless	MERRA2	0.625°×0.5°/10km	1 hourly
Reanalysis	ts1	soil temperature	° C	MERRA2	0.625°×0.5°/10km	1 hourly
Reanalysis	ts2	soil temperature	° C	MERRA2	0.625°×0.5°/10km	1 hourly
Reanalysis	ts3	soil temperature	° C	MERRA2	0.625°×0.5°/10km	1 hourly
Remote Sensing	sm_s_wetness	surface soil wetness	unitless	SPL4SMGP.007	9 km	3 hourly
Remote Sensing	sm_r_wetness	rootzone soil wetness	unitless	SPL4SMGP.007	9 km	3 hourly
Remote Sensing	sm_p_wetness	profile soil wetness	unitless	SPL4SMGP.007	9 km	3 hourly
Remote Sensing	nbar1	red band	unitless	MCD43A4v061	500 m	daily
Remote Sensing	nbar2	near infrared 1 band	unitless	MCD43A4v061	500 m	daily
Remote Sensing	nbar3	blue	unitless	MCD43A4v061	500 m	daily
Remote Sensing	nbar4	green	unitless	MCD43A4v061	500 m	daily
Remote Sensing	nbar5	near infrared 2 band	unitless	MCD43A4v061	500 m	daily
Remote Sensing	nbar6	shortwave infrared 1 band	unitless	MCD43A4v061	500m	daily
Remote Sensing	nbar7	shortwave infrared 2 band	unitless	MCD43A4v061	500 m	daily
Remote Sensing	slope	terrain slope	radian	Geomorpho90m	90 m	static
Remote Sensing	spi	stream power index	unitless	Geomorpho90m	90 m	static
Remote Sensing	cti	compound topographic index	unitless	Geomorpho90m	90 m	static

344

2.3 Machine learning model

2.3.1 General model design

347 We used an RF regression algorithm to train site-level and grid-level ML models (Kim et al.,
348 2020). RF regression builds an assembly of independent trees, each of which is trained from a
349 random subset of input data and tested against the rest of the data (Breiman, 2001). A tree
350 grows two leaves when a random selection of subset features reduces the mean squared error

351 (MSE) of predictions after splitting at a leaf node. Each tree is trained on a bootstrap sample of
352 input data. Trees constructed in this way are less correlated in the ensemble. The generalization
353 error converges as the forest grows to a limit to avoid overfitting. Compared to other ML
354 algorithms, RF has shown to have better accuracy and lower uncertainty (Irvin et al., 2021; Kim
355 et al., 2020). This approach has been previously applied to upscaling CH_4 fluxes in wetlands
356 and rice paddies across multiple ecosystems (Davidson et al., 2017; Feron et al., 2024; McNicol
357 et al., 2023; Ouyang et al., 2023; Peltola et al., 2019).
358
359 A grid-search hyperparameter tuning for daily models was performed before predictor selection.
360 We carried out analyses in Python version 3.6 with the ensemble RF regressor in package
361 'scikit-learn' (Pedregosa et al., 2011). With all the predictors and data, hyper-parameters were
362 set after tuning for optimized model performance, including the number of trees
363 (n_estimators=100), number of variables to consider when looking for the best split
364 (max_features="sqrt", meaning the square root of the total number of feature variables), the
365 maximum depth of the tree (max_depth=10), the minimum number of samples required to split a
366 node (min_sample_split=10), and the minimum number of samples at a leaf node
367 (min_samples_leaf=4).
368
369 For predictor selection and comparisons between the site-level model using *in-situ* variables
370 and the grid-level model using gridded versions of *in-situ* variables, we built the model across all
371 sites and adopted 5-fold cross-validation and 'out-of-bag' scores from ensemble trees to
372 evaluate model performance, because, at this stage, we aimed to find physically reasonable
373 variables from *in-situ* measurements and to compare how the differences in scales and
374 measuring methods between *in-situ* predictors and gridded proxies affect model learned
375 temporal variability in CH_4 fluxes. A subset of data was bagged to train each tree in the RF
376 model, with the rest out-of-bag data used as independent validation data to evaluate the
377 prediction accuracy of each tree, resulting in the average out-of-bag scores of all the trees in the
378 model. Cross-validation was applied to daily predictions to select variables that can best predict
379 the daily variability of CH_4 fluxes within sites. The changes in model performance after predictor
380 selection and after switching from site-level variables (*in-situ* measurements) to grid-level
381 proxies (reanalysis data) were assessed, which helped quantify differences in model
382 performance when modeling on *in-situ* measured predictor variables versus modeling on
383 substitute variables at grid level.
384
385 A summary of input variables for grid-level modeling is provided in Table 1. Although RF can
386 enhance model robustness when collinearity presents in input variables, the collinearity could
387 affect the interpretation of feature importance measured by impurity decrease in RF models.
388 Therefore, we first built a baseline grid-level model with independent variables after a pairwise
389 Pearson correlation test (Fig. S14) to exclude covariates. The resulting baseline features
390 included air pressure (pa), latent heat flux (le), sensible heat flux (h), soil temperature (ts2),
391 rootzone soil wetness (sm_r_wetness), slope, spi, and cti. Then we designed four additional
392 different model settings by changing predictor variables, including (1) baseline variables plus
393 covariates, (2) only variables from MODIS NBAR, (3) baseline variables plus NBAR bands, and
394 (4) all predictor variables. In this forward feature selection process, we evaluated the impacts of

395   adding constraint variables from remote sensing products on model performance. Model
396   predictive performance evaluates the accuracy of a model to predict at a new site without any
397   prior knowledge. For the spatial predictive performance evaluation of grid-level ML models, we
398   used a nested leave-one-site-out cross-validation scheme (LOOCV, hereafter). Such a scheme
399   selects one site to use as independent validation data to evaluate models trained and tested
400   with data from the remaining sites, repeating the process for all sites. Without any prior
401   knowledge of the validation site added to a model, the LOOCV scheme can assess the
402   predictive ability of the model in a new place as well as evaluate the uniqueness of a site in the
403   dataset. Similar forms of spatial LOOCV have been used to evaluate upscaling models for
404   global or regional CO_2 and CH_4 (McNicol et al., 2023; Peltola et al., 2019; Virkkala et al., 2021).
405   The validation of the upscaling model was not only performed with respect to daily predictions,
406   but also on monthly means. The predictive performance of the upscaling model on monthly
407   variability of CH_4 fluxes and spatial variability across sites is important for studies that vary in
408   temporal and spatial scales.
409
410   Model predictive performance was assessed using three evaluation metrics: mean absolute
411   error (MAE), root mean squared error (RMSE), and R^2 score. Daily modeled CH_4 fluxes were
412   compared to EC observations at each validation site. The evaluation metrics were calculated at
413   daily and monthly scales for each site separately to examine the model performance by general
414   wetland types and for all sites pooled together to evaluate the overall performance and compare
415   with existing studies. Squared error metrics are more sensitive to outliers and highly skewed
416   data, which is often the case with CH_4 fluxes. Therefore, we selected both MAE and RMSE to
417   quantify the errors. The mean error (ME) between model predictions and validation data was
418   calculated, representing systematic bias in predicted fluxes. The standard deviation of model
419   residuals was also included to measure the spread of the residuals. This matches RMSE when
420   ME equals zero.
421
422   Two additional ML algorithms were compared with RF: SVM and ANN. SVM is efficient with
423   sparse data where the dimension of the input space is greater than the number of training
424   samples (Kuter, 2021). While the training process of ANN is expensive and time-consuming, it
425   can develop deep networks with growing training data which may increase predictive
426   performance (Saikia et al., 2020). We used support vector regression to model CH_4 fluxes with
427   the same predictor variables and dataset as used in ensemble RF regressions. Multilayer
428   perceptron regressor is an implementation of an ANN model that adjusts the weights of neurons
429   using backpropagation to improve prediction accuracy. It uses the square error as the loss
430   function and a stochastic gradient-based optimizer 'adam' for weight optimization. We used two
431   hidden layers in the ANN model, each with 50 neurons. Data from all variables were normalized
432   to achieve the best model performance of SVM and ANN.

433 ## 2.3.2 CH_4 flux upscaling

434   We trained 500 ensemble RF models with predictors of grid-level models from the general
435   model design and with data from all sites for upscaling daily CH_4 fluxes. Each RF model was
436   trained with the same optimized hyper-parameters and different bootstrap samples. Ensemble
437   models were then applied to 0.098° gridded predictors to produce the upscaling CH_4 flux

438   intensities from the means of the 500 predictions and the prediction uncertainty from the
439   standard deviations. Given that the CH_4 fluxes were modeled with data from the wetland EC
440   sites, a wetland extent map was also needed to constrain the areas when scaling grid emissions
441   (see section 2.4). Final CH_4 emission and uncertainty maps associated with wetland extents
442   were the results of multiplying the predicted means and standard deviations of flux intensities
443   with wetland areas. All wetland maps were resampled to 0.098° x 0.098° resolution with a
444   conservative remapping method for producing the emission products.

445 2.4 Wetland extent maps and benchmark estimates of wetland
446 CH_4 emissions

447   Wetland extent maps were applied to scale the modeled CH_4 flux intensities to the region. The
448   Wetland Area and Dynamics for CH_4 Modeling (WAD2Mv2), representing spatiotemporal
449   patterns of inundated vegetated wetlands at 0.25° resolution, was selected as the reference for
450   dynamic wetland areas in this study (Z. Zhang et al., 2021). Active and passive microwave
451   detected inundation combined with static wetlands were used to delineate the monthly dynamics
452   of wetland inundation between 2000 and 2020. Open water bodies such as lakes, rivers,
453   reservoirs, coastal wetlands, and rice paddies were excluded. We used monthly mean WAD2M
454   fractions between 2010 and 2020 to represent seasonal wetland dynamics. Emission
455   estimations are subject to differences in the wetland extent between maps (Saunois et al.,
456   2020). We used monthly means of the Global Inundation Extent from Multi-Satellites (GIEMS2)
457   product (Prigent et al., 2020) to represent temporal patterns of the restricted wetland extents at
458   0.25° resolution. The coarse resolution maps were resampled to 0.098° x 0.098° grids using the
459   nearest neighbor method. The static Global Lakes and Wetlands Database version 1 (GLWDv1)
460   Level 3 1-km resolution map excluding classes of lakes, rivers, and reservoirs (Lehner & Döll,
461   2004) was included to quantify the upper limit of wetland cover. For all explicit GLWDv1 wetland
462   classes, we assumed a 100% wetland coverage in the original pixels, except for 'intermittent
463   wetland/lake' for which we assumed a 50% coverage; for GLWDv1 classes represented as
464   extent ranges, we used the average value of the range (i.e., 75% for 50-100% wetland, 37% for
465   25-50% wetland, and 12% for 0-25% wetland). To support domain emission comparisons,
466   wetland cover was also extracted from the updated GLWD version 2 dataset (GLWDv2, Lehner
467   et al., 2024) which provides the spatial extent of 33 waterbody and wetland classes at 500-m
468   spatial resolution. All freshwater wetland classes that occur in our study area (classes 8-25)
469   from GLWDv2 were included (i.e., excluding rivers, lakes, reservoirs and other permanent open
470   water bodies, as well as coastal saline/brackish wetlands). The original wetland areas per
471   GLWDv2 pixel were summed across all included classes to derive a total wetland area per pixel.
472   Furthermore, a regional freshwater wetland distribution dataset was calculated from a
473   permafrost region specific land cover map (CALU - circum-Arctic landcover units) which
474   classified 23 land covers including 3 wetland classes and 10 moist to wet tundra classes at 10-
475   m resolution and aggregated to 1km with the majority class (Bartsch et al., 2024). This regional
476   wetland map was applied for CH_4 emission estimation in the North Slope region in Alaska to
477   assess the impacts of different wetland maps on emission estimates in this area when
478   compared against airborne measurements. Wetland areas from the finer resolution maps were
479   aggregated to 0.098° x 0.098° grids for emission calculations.

480

481 We compared WetCH$_4$ emissions with benchmark domain or regional estimates from bottom-up

482 process models, top-down atmospheric observation-based inversions, and existing upscaling

483 studies. We acquired data for the study domain from the ensemble mean of bottom-up process-

484 based models from the Global Carbon Project (GCP) (Z. Zhang, Bansal, et al., 2023) and the

485 extended ensemble of wetland CH$_4$ estimates that were priors for the top-down GEOS-Chem

486 atmospheric chemical and transport model (WetCHARTs) (Bloom et al., 2017; Friedlingstein et

487 al., 2022). We also included the atmospheric inversions of northern high latitudes from an

488 assimilation CarbonTracker-CH$_4$ system (Bruhwiler et al., 2014; update at

489 https://gml.noaa.gov/ccgg/carbontracker-ch4/carbontracker-ch4-2023/). We compared WetCH$_4$

490 with existing upscaled products of monthly CH$_4$ wetland fluxes based on Peltola et al. (2019) for

491 the study domain. For regional wetland hotspots, CH$_4$ flux estimates were obtained from Carbon

492 in Arctic Reservoirs Vulnerability Experiment (CARVE), which measured total atmospheric

493 columns of CO$_2$, CH$_4$, and carbon monoxide over North Alaska in spring, summer, and early fall

494 between 2012 and 2014 (R. Y.-W. Chang et al., 2014; Miller et al., 2016). These were used to

495 verify our seasonal emission estimates over the North Slope region (Zona et al., 2016).

496 3. Results

497 3.1 Model validation

498 3.1.1 Site-level modeling

499 Site-level modeling used all wetland sites to build a RF model and identified the 10 most

500 important variables measured *in situ* that, if left out, decreased the valuation score of the model

501 by more than 90% based on the mean decrease in impurity (Fig. S3). With bootstrap sampling

502 and using all candidate predictors (Fig. 1) in the model, the out-of-bag RMSE of the site-level

503 model was 30.22 nmol m^{-2} s^{-1}, and the out-of-bag R^2 between observed daily means of CH$_4$

504 fluxes and prediction was 0.73. Modeling with the 10 most important variables at site level

505 resulted in similar model performance, with an out-of-bag RMSE of 30.43 nmol m^{-2} s^{-1} and an

506 out-of-bag R^2 of 0.73. We then tested building separate models according to wetland types

507 because distinct CH$_4$ fluxes have been observed from wet tundra (Fig. S4, mean ± standard

508 deviation: 13 ±14 nmol m^{-2} s^{-1}), bogs (22 ±26 nmol m^{-2} s^{-1}) and fens (56 ±88 nmol m^{-2} s^{-1}). The

509 out-of-bag R^2 (RMSE) was 0.85 (7.2 nmol m^{-2} s^{-1}) for bog, 0.84 (27.7 nmol m^{-2} s^{-1}) for fen, and

510 0.57 (34.3 nmol m^{-2} s^{-1}) for wet tundra. Modeling with the selected 10 predictors resulted in an

511 out-of-bag R^2 (RMSE) of 0.84 (7.6 nmol m^{-2} s^{-1}) for bog, 0.84 (27.9 nmol m^{-2} s^{-1}) for fen, and for

512 0.53 (36.3 nmol m^{-2} s^{-1}) wet tundra. Next, we tested whether the inclusion of non-wetland sites

513 (upland and rice sites) would affect model performance. This resulted in an out-of-bag R^2

514 decrease to 0.56 and RMSE increase to 38.86 nmol m^{-2} s^{-1}, which suggests that a generalized

515 ML model over all land cover classes is not practical to reliably predict CH$_4$ fluxes with the

516 current set of predictors and available data. This is most likely due to the distinctive features of

517 CH$_4$ emissions between wetlands and non-wetland classes (Fig. S4).

3.1.2 Grid-level modeling and remote sensing constraints

Substituting *in-situ* measurements of selected predictor variables with gridded MERRA2 variables slightly reduced model accuracy. The out-of-bag R^2 decreased by 9.6% to 0.65 and RMSE increased by 15% to 34.9 nmol m^{-2} s^{-1} compared to the site-level model. The coarse resolution MERRA2 reanalysis data captures less spatial variability of the selected physical variables and is less accurate at the grid-level compared to *in situ* EC measurements.

Adding remote sensing constraints to the gridded variables can improve model predictive performance and reduce errors. Modeling on baseline features explained on average 46% of daily CH$_4$ fluxes' variability in validation sites with the largest range of errors (Fig. 3a). The medians in the baseline model of R^2, MAE, RMSE, ME under the LOOCV scheme were 0.5, 16.4 nmol m^{-2} s^{-1}, 21.0 nmol m^{-2} s^{-1} and 6.4 nmol m^{-2} s^{-1}, respectively. Adding NBAR or covariates from MERRA2 and SMAP input variables returned a higher mean R^2 or slightly lower mean errors than the baseline model, whereas modeling with all gridded input variables (the 'all' model setting) achieved the highest mean R^2 of 0.51 with the comparable mean MAE (23.6 nmol m^{-2} s^{-1}), RMSE (32.1 nmol m^{-2} s^{-1}) and ME (0.9 nmol m^{-2} s^{-1}) (Table S4). Our results suggest that including remote sensing constraints or covariates improved models' ability to predict spatial variability in wetland CH$_4$ fluxes and reduced prediction errors. These results confirm our selection of predictor variables for the upscaling model (Table 1).

The average importance of the baseline features shows their influence on the grid-level model predictive performance (Fig. 3b). Importance of independent predictors under LOOCV scheme, though slightly varied between models, agreed in selecting MERRA2 soil temperature (ts2) as the primary driver in predicting daily CH$_4$ fluxes in northern wetlands, followed by SMAP rootzone wetness (sm_r_wetness). The eight baseline features accounted for a 99% reduction in the mean validation score of the baseline models. Nevertheless, all variables contributed to predicting variability in CH$_4$ fluxes, showing the complexity of environmental factors that would affect the rates of CH$_4$ production and the process of gas exchange.
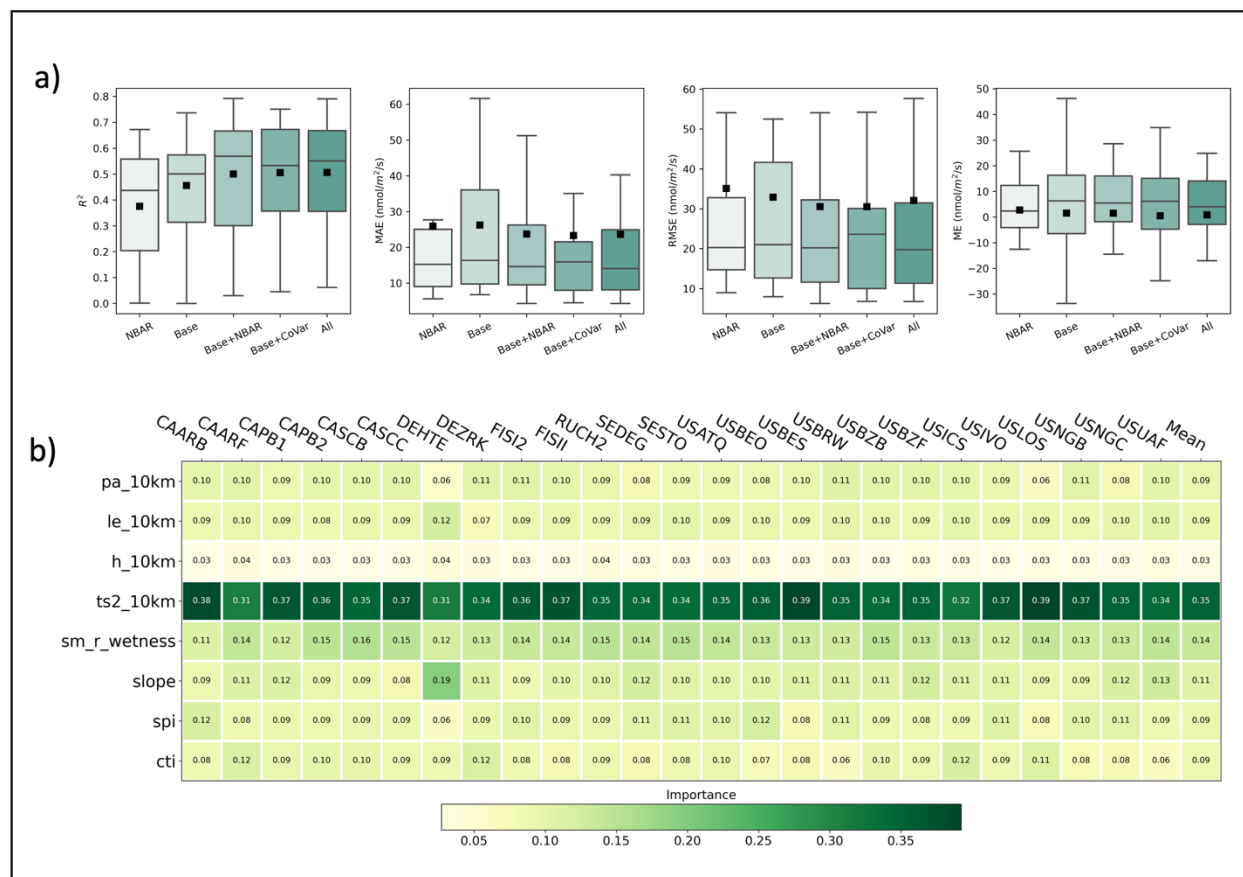
Fig. 3 Grid-level modeling: a) Distribution of R^2, MAE, RMSE, and ME for all sites (size = 25) in a LOOCV scheme based on gridded data using five model settings: RF modeled using only MODIS NBAR bands, baseline features (MERRA2 air pressure, latent heat flux, sensible heat flux, soil temperature, SMAP rootzone soil wetness, topographic slope, spi, and cit), baseline features plus MODIS NBAR bands, baseline features plus correlated variables within the MERRA2 and SMAP dataset, and all gridded input variables together. The model settings are ranked by mean R^2, from lowest (left) to highest (right); b) Mean variable importance of baseline models (last column) in the LOOCV scheme and at each site (columns labeled with validation site ID). The values in each column are the means of accumulation of the impurity decrease when a variable was taken out in the trees of a RF model, representing the importance of such variable to the model. The variable names and descriptions refer to Table 1.

Daily mean CH_4 fluxes exhibited great variability in wetlands across space and time (mean = 35 nmol m^{-2} s^{-1}, σ = 65 nmol m^{-2} s^{-1}, Fig. S3). The model predictive performance (Fig. 4) was calculated for each site and the average performance on the daily variability in CH_4 fluxes was best at wet tundra sites with a mean R^2 of 0.56, followed by bog sites (0.51) and fen sites (0.45). Due to the large variability in fen daily fluxes, errors of daily predictions were highest in fen sites (mean RMSE = 54.2 nmol m^{-2} s^{-1} and mean MAE = 37.8 nmol m^{-2} s^{-1}), followed by bog sites (mean RMSE = 27.6 nmol m^{-2} s^{-1} and mean MAE =22.5 nmol m^{-2} s^{-1}), and were lowest in wet tundra sites (mean RMSE = 13.5 nmol m^{-2} s^{-1} and mean MAE =10.3 nmol m^{-2} s^{-1}). Our model slightly overestimated daily fluxes (mean ME = 0.9 nmol m^{-2} s^{-1}) was driven by underestimation

570 of fen sites (mean ME = -12 nmol m^{-2} s^{-1}) versus overestimation of bog (mean ME = 14 nmol m^{-2}
571 s^{-1}) and wet tundra (mean ME = 3 nmol m^{-2} s^{-1}) sites.
572
573 Model predictive performance on aggregated monthly means of CH$_4$ fluxes increased by 37%
574 as compared to daily means (mean R^2 = 0.70, Fig.4, Table S4). This improvement may be
575 attributed to a better representation of the environmental conditions' average state over a month
576 by the input variables compared to the daily variability. Performance was higher in wet tundra
577 (mean R^2 = 0.73) and bogs (mean R^2 = 0.73) and lower in fen sites (mean R^2 = 0.64, Fig. 4).
578 Mean errors in monthly mean predictions were: RMSE = 28.1 nmol m^{-2} s^{-1}, MAE = 21.4 nmol m^{-2}
579 s^{-1}, and ME = 0.37 nmol m^{-2} s^{-1} (Table S4). Prediction residuals of daily and monthly CH$_4$ fluxes
580 (Fig. S6) showed normal distributions for wet tundra sites, indicating the spread of residuals
581 were random errors that increased with the flux magnitude. The residuals had a skewed normal
582 distribution for bog sites indicating likely overestimation. The long-left tails in prediction residuals
583 indicated that the intense emission fluxes from fens during summer peaks were underestimated
584 (Fig. S6).
585
586 Site-by-site validation of daily flux predictions varied greatly between individual sites (Fig. 5, S7).
587 For example, US-UAF, an EC site in Interior Alaska with mature black spruce cover and full
588 understory vegetation and mosses over permafrost (Ueyama, Iwata, et al., 2023), which is the
589 only one of the five forest bog sites in our dataset that had low CH$_4$ fluxes and weak seasonal
590 cycles (less than 10 nmol m^{-2} s^{-1}), was significantly overestimated by our model (RMSE = 58
591 nmol m^{-2} s^{-1} and MAE = 53 nmol m^{-2} s^{-1}). Permafrost presence and ground water below soil
592 surface may explain the low fluxes at this site (Iwata et al., 2015; Ueyama, Knox, et al., 2023).
593
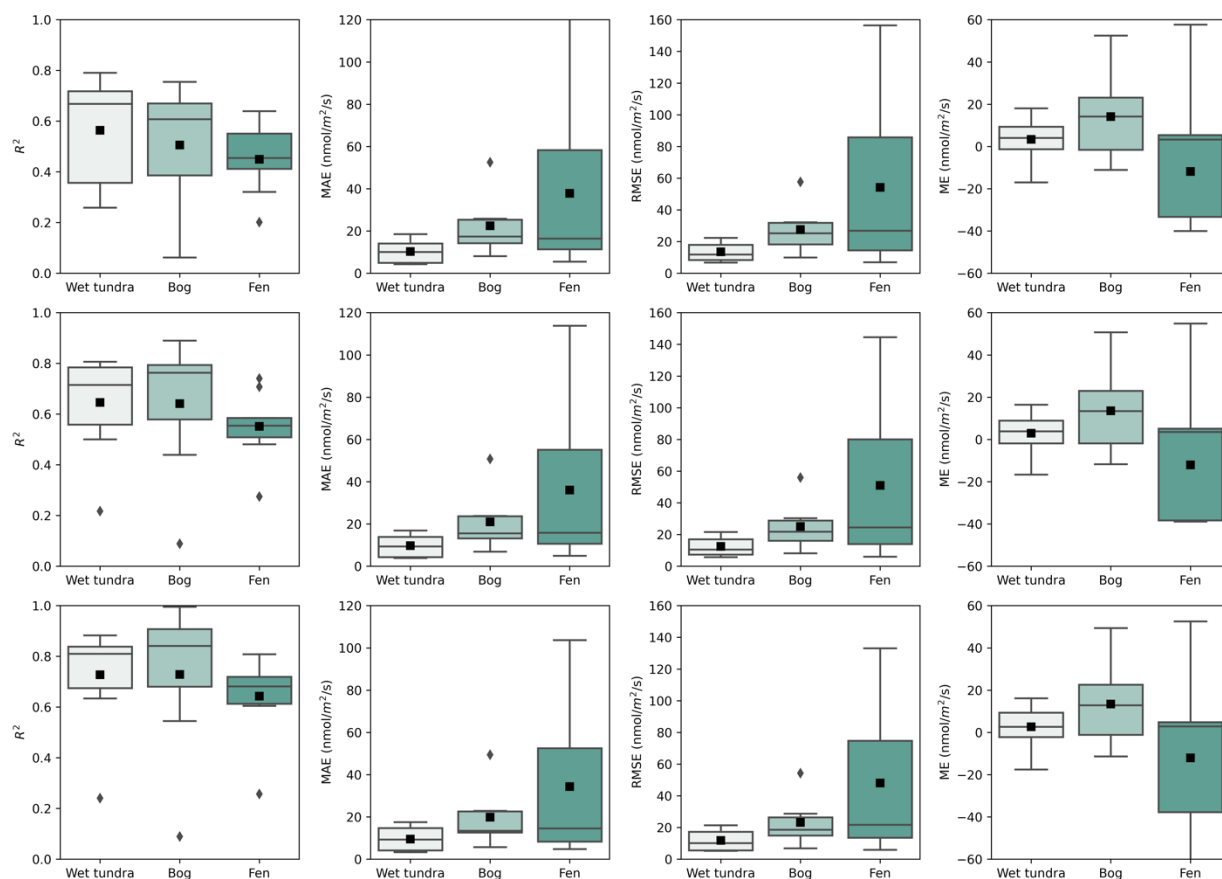
594
595
596 Fig. 4 Model predictive performance evaluation on RF modeled CH$_4$ fluxes at grid level under
597 LOOCV scheme: boxplots of R^2, MAE, RMSE, and ME across validation sites by wetland types
598 with mean values denoted in black squares at daily/weekly/monthly (top/middle/bottom panel)
599 time steps.
600
601
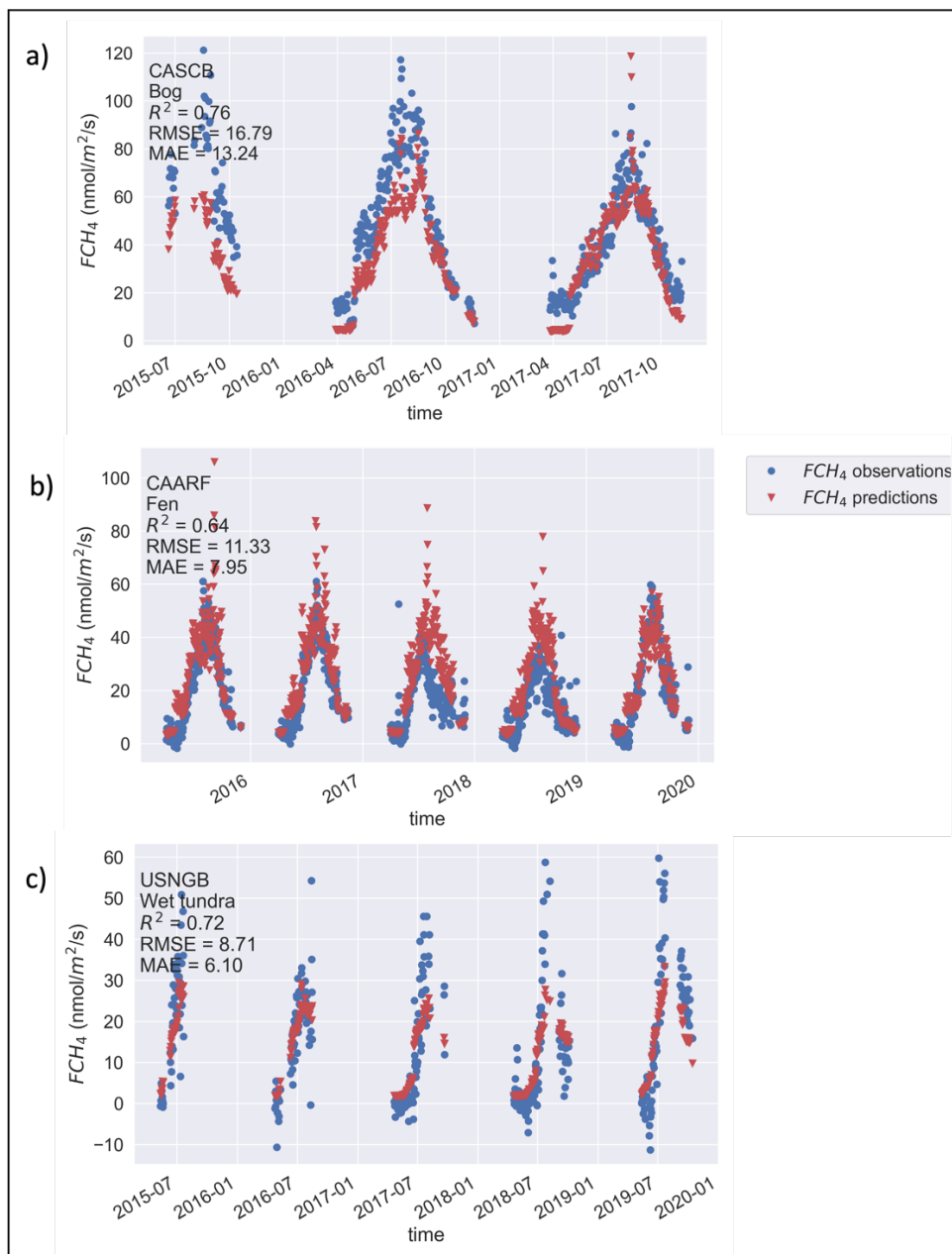
602
603
604 Fig. 5 Example model predictive performance in seasonal cycles of daily FCH₄ at the validation
605 sites of CA-SCB, CA-ARF, and US-NGB, representing bog, fen, and wet tundra, respectively.
606

3.2 Upscaled wetland CH$_4$ emissions

3.2.1 Wetland area weighted CH$_4$ emissions

609 Upscaled daily CH$_4$ fluxes were weighted by wetland fraction to estimate gridded daily CH$_4$
610 fluxes from northern wetlands based on WAD2Mv2, GIEMS2, and GLWDv1 between 2016 and

611 2022 (Fig. 6), and GLWDv2 for comparison. The mean annual emissions and RF model
612 associated uncertainties are summarized with different wetland maps in Table S3. The estimate
613 from WetCH$_4$ with WAD2Mv2 was 22.8 ±2.4 Tg CH$_4$ yr^{-1}, comparable to UpCH$_4$ (23.5 ±5.8 Tg
614 CH$_4$ yr^{-1}). With GIEMS2, WetCH$_4$ estimated the minimum annual emission of 15.7 ±1.8 Tg CH$_4$
615 yr^{-1}. With GLWDv1 and GLWDv2, WetCH$_4$ estimated potential annual emissions of 46.0 ±5.1 Tg
616 CH$_4$ yr^{-1} and 51.6 ±2.2 Tg CH$_4$ yr^{-1} for 2016-2022, respectively. The spatial patterns were similar
617 to the post 2016 mean annual fluxes from the GCP process-model ensemble means (28.6
618 ±21.6 Tg CH$_4$ yr^{-1} for 2016-2020), WetCHARTs (29.5 ±30.0 Tg CH$_4$ yr^{-1} for 2016-2019), and
619 atmospheric inversions of CarbonTracker-CH$_4$ (40.9 Tg CH$_4$ yr^{-1} for 2016-2022), highlighting the
620 high emission areas in the Hudson Bay Lowlands and West Siberian Lowlands. The emissions
621 from WetCH$_4$-GIEMS2 were lower in these two hotspots than other estimates. Differences in the
622 distribution of CH$_4$ emissions between wetland products reflect the influence of wetland
623 dynamics. Mean monthly wetland inundations are provided by WAD2Mv2 and GIEMS2, which
624 set the dynamic limits for the wetland boundaries of the CH$_4$-emitting surface. While emissions
625 resulting from inundation were captured, it appeared that saturated or wet subsoil conditions
626 were not well represented by WAD2M and GIEMS2, resulting in low emissions in wet yet non-
627 inundated tundra (i.e., Alaska North Slope). To address this, we incorporated wetland fractions
628 from the CALU high-resolution wetland map (Bartsch et al., 2024) specifically produced for the
629 permafrost region in order to estimate Alaska North Slope emissions. Wetland fractions from
630 GLWD (both v1 and v2) represent a static maximum wetland distribution throughout time. Thus,
631 estimates from GLWD may represent the upper bounds for all northern wetlands under
632 contemporary conditions.

633

634

635
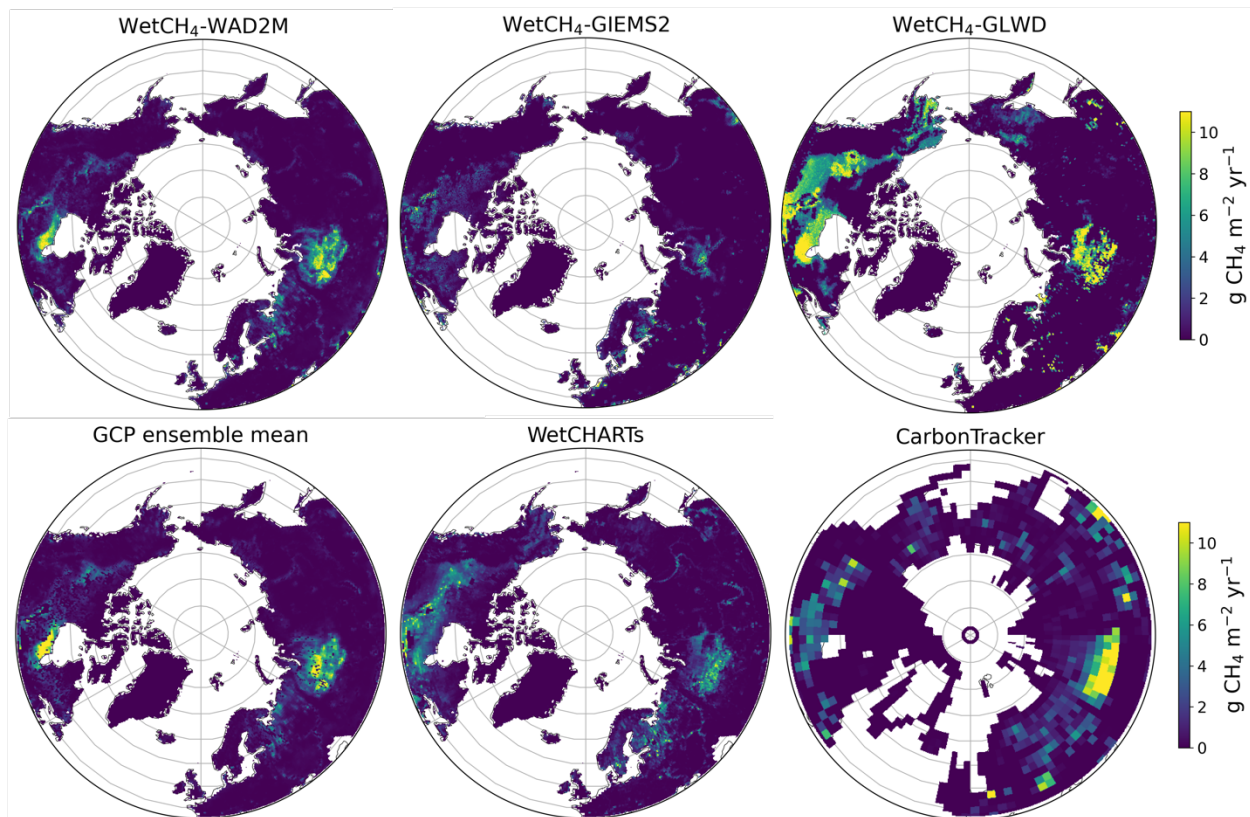
636 Fig. 6 Mean annual wetland CH_4 fluxes: the top row contains WetCH4 upscaled fluxes between
637 2016 and 2022 and weighted by wetland fractions for three wetland maps WAD2Mv2, GIEMS2,
638 and GLWDv1; the bottom row contains bottom-up GCP ensemble mean, WetCHARTs, and top-
639 down estimates of CarbonTracker-CH_4 natural microbial emissions.

640

641 We compared spatial distributions of our upscaled fluxes (WetCH4) with two alternative
642 upscaled datasets. Using the same wetland weights, our product showed similar spatial patterns
643 to UpCH4 (McNicol et al., 2023) and the upscaled fluxes from Peltola et. al. (2019) (Fig. S9).
644 Spatially, the maximum mean flux of 2016-2022 for WetCH4 with WAD2Mv2 was 69 mg CH_4 m^{-2}
645 day^{-1}, UpCH4 produced a maximum mean flux between 2016-2018 of 88 mg CH_4 m^{-2} day^{-1}.
646 While all three products predicted concentrated CH_4 exchange in the Hudson Bay Lowlands and
647 West Siberian Lowlands, and low fluxes in West Canadian Arctic tundra, WetCH4 predicted
648 lower fluxes in forested wetlands of West Canada than UpCH4 (Fig. S9 a,b). With GLWDv1,
649 WetCH4 predicted similar fluxes to those of Peltola et al. (2019), with the exception of a number
650 of potent emitting grids in the West Siberian Lowlands (Fig. S9 c,d) and a maximum mean flux
651 of 132 mg CH_4 m^{-2} day^{-1} from WetCH4.

652 ## 3.2.2 Seasonal cycles of wetland CH_4 emissions

653 Mean seasonal cycles of wetland CH_4 emissions were consistent with bottom-up estimates in
654 the domain and top-down inversions in high latitudes (Fig. 7). The amplitudes of two ML-based
655 estimates agreed in the domain (WetCH4 and UpCH4 both within WAD2Mv2 wetland areas) and
656 were lower than the ensemble means of GCP or WetCHARTs estimates during the growing
657 season (Fig. 7a). In the northern high latitudes (60° - 90° N), the amplitudes of this study closely
658 agree with WetCHARTs, and both were lower than the ensemble means of GCP in the growing
659 season (Fig. 7b). Our emissions in June-July-August were lower than the emissions attributed
660 by the atmospheric inversion of CarbonTracker-CH_4, which does not discriminate between
661 wetland and open water sources. We did not use comparisons with CarbonTracker-CH_4 for 45°-
662 90° due to likely considerable contributions from aquatic systems and other non-wetland factors
663 in the inversion estimates. Notably, uncertainties between ML-based approaches with the same
664 wetland extents showed less variation than those between process-based models, especially
665 during the growing season. The phase of our estimates (WetCH4) agreed with bottom-up and
666 top-down models, peaking in July followed by August (Fig. 7a,b), whereas UpCH4 showed a
667 month lag, probably due to the two- or three-week lag of predictor variables selected in UpCH4
668 (McNicol et al., 2023). Peak fluxes in July and August were commonly seen in tower
669 measurements.

670

671 The seasonality in upscaled wetland CH_4 emissions corresponded to the intensities of fluxes
672 and dynamics of wetland areas. We compared mean seasonal cycles of upscaled products with
673 different dynamic or static wetland maps to constrain the impacts of wetland areas (Fig. 7c). As
674 observed in spatial distributions (Fig. 7a,c), emissions from the potential emitting surface
675 (WetCH4_GLWDv1) were 95% higher than those from reference inundated wetlands
676 (WetCH4_WAD2Mv2) during the growing season, and doubling in winter. Within the GLWDv1
677 emitting surface, WetCH4 predicted higher emissions than Peltola et al. (2019) in July (43%),

678 August (43%), December (41%), and January (61%), but 15% lower in October. We decoupled
679 the mean annual seasonal cycle for WAD2M from the emission seasonality by using a fixed
680 maximum WAD2M extent. The resulting seasonal emissions primarily driven by soil
681 temperatures and moisture manifested elevated emissions in all months and an intensified
682 seasonal cycle. Reported emissions (Zona et al., 2016) and large bursts (Mastepanov et al.,
683 2008) from the freezing active layer at permafrost areas in October (zero-curtain period) may
684 not be well captured by our ML model. The differences in wetland areas between the two
685 dynamic products (WAD2Mv2 and GIEMS2) mostly affected emissions in May and June in
686 WetCH$_4$, but significantly affected emission magnitudes in UpCH$_4$. Despite the differences in
687 wetland areas, the phases of emissions cycles of WetCH$_4$ were consistent with those from
688 Peltola et al., whereas UpCH$_4$ again lagged a month.
689
690 We compared upscaled seasonal cycles with CH$_4$ fluxes estimated from regional airborne
691 measurements taken during CARVE campaigns over the Alaska North Slope (Fig. 7d). Given
692 that the wetland area in this region is uncertain (Miller et al., 2016), we computed mean
693 seasonal cycles over the land assuming all land in this area is water saturated in the soil, over
694 freshwater wetlands of CALU, and over WAD2M and Hydrolakes, representing three different
695 scenarios. In the lowland area of the North Slope (74295 km^2 spanning between 69.8°N -
696 71.4°N, 164.4°W - 152.7°W), the wetland area was estimated at 10611 km^2 from CALU, 4800
697 km^2 from GLWDv2, and 4049 km^2 from the maximum extent month in July of WAD2Mv2,
698 respectively. The range of our upscaled estimates aligned with regional emissions derived from
699 CARVE measurements. Chang et al. (2014) estimated 7 ±2 mg CH$_4$ m^{-2} d^{-1} of mean CH$_4$ fluxes
700 during the growing season in the North Slope from the column analysis of CARVE data. The
701 mean fluxes (May to September) of WetCH$_4$ with CALU were estimated at 7.3 ±0.8 mg CH$_4$ m^{-2}
702 d^{-1} (5.5 ±0.6 mgC CH$_4$ m^{-2} d^{-1}), which is within the range of various CARVE estimations (Miller et
703 al., 2016). The landscape is in the biome of the Arctic coastal tundra and is covered by sedges,
704 grasses, mosses, and dwarf shrubs. A large number of lakes and freshwater ponds are
705 scattered across the area. Studies at the West Alaska lowland of Yukon–Kuskokwim Delta
706 found aquatic fluxes that were about ten times higher than in wet tundra during September
707 (Ludwig et al., 2023), suggesting that a major source of the airborne fluxes missing in WetCH$_4$ in
708 the late growing season, can be attributed to open water fluxes. Remarkable increases could be
709 in summer and winter if we assume wetland over this region, as indicated by the range between
710 the green and the black lines in Fig. 8d. Yet, future emissions due to permafrost thaw still
711 depend on the hydrological changes of the landscape.
712
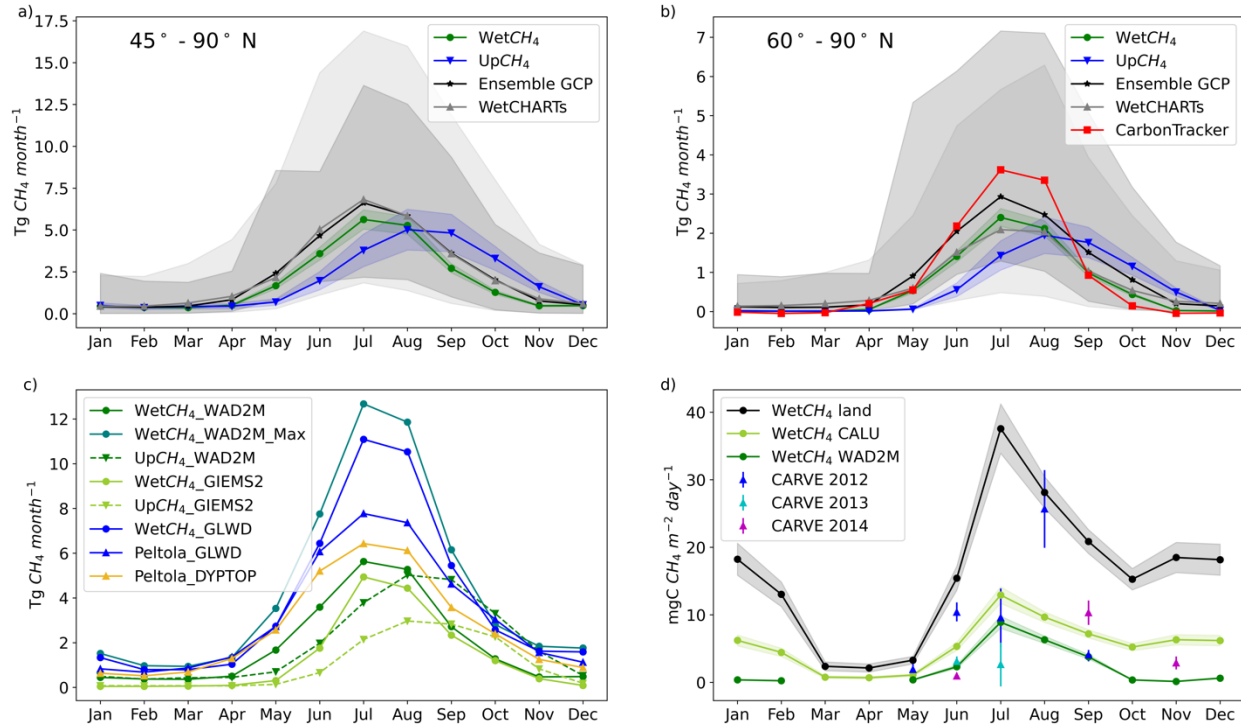
713
714 Fig. 7 Multi-year average seasonal cycles of wetland CH₄ emissions: (a) comparison of ML
715 upscaled mean seasonal cycles in reference wetland areas (WAD2Mv2) with the cycles from
716 process-based models in the northern mid-high latitudes (45° - 90° N); (b) same comparison for
717 northern high latitudes (60° - 90° N) and addition of atmospheric CarbonTracker-CH₄ attributed
718 microbial emissions (2016-2022); (c) comparison of three ML upscaled mean seasonal cycles of
719 CH₄ emissions with different wetland area maps (WAD2Mv2, WAD2Mv2 maximum extent,
720 GIEMS2, GLWDv1); (d) comparison of WetCH₄ mean seasonal cycles over the land (black line),
721 weighted by wetland of the CALU map (olive line), or weighted by fractions of WAD2Mv2 (green
722 line), with estimates of CH₄ fluxes in growing seasons from CARVE retrievals in North Slope
723 area of Alaska (Zona et al., 2016).

724

725 3.2.3 Interannual variations in wetland CH₄ emissions

726

727 The mean annual emissions from ML-based estimates with WAD2M were lower than the GCP
728 ensemble mean and WetCHARTs over different years from 2016 forward (Fig. 8a). All products
729 demonstrated similar emission patterns for the domain in the interannual trends and variations,
730 highest in 2016 and lower for three years from 2017 to 2019 (Fig. 8). The interannual variations
731 in WetCH₄ were driven by the interannual variability in the upscaled fluxes as only multi-year
732 mean seasonal dynamics from WAD2Mv2 were used. All products identified intensified
733 emissions in 2016 as indicated by the variations relative to period means (Fig. 8b). Higher than
734 period average emissions in 2020 were also modeled by WetCH₄ and ensemble GCP. The
735 recent intensification from wetland emissions was discovered globally with an important

736 contribution from northern wetlands (S. Peng et al., 2022; Yuan et al., 2024; Z. Zhang, Poulter,
737 et al., 2023).
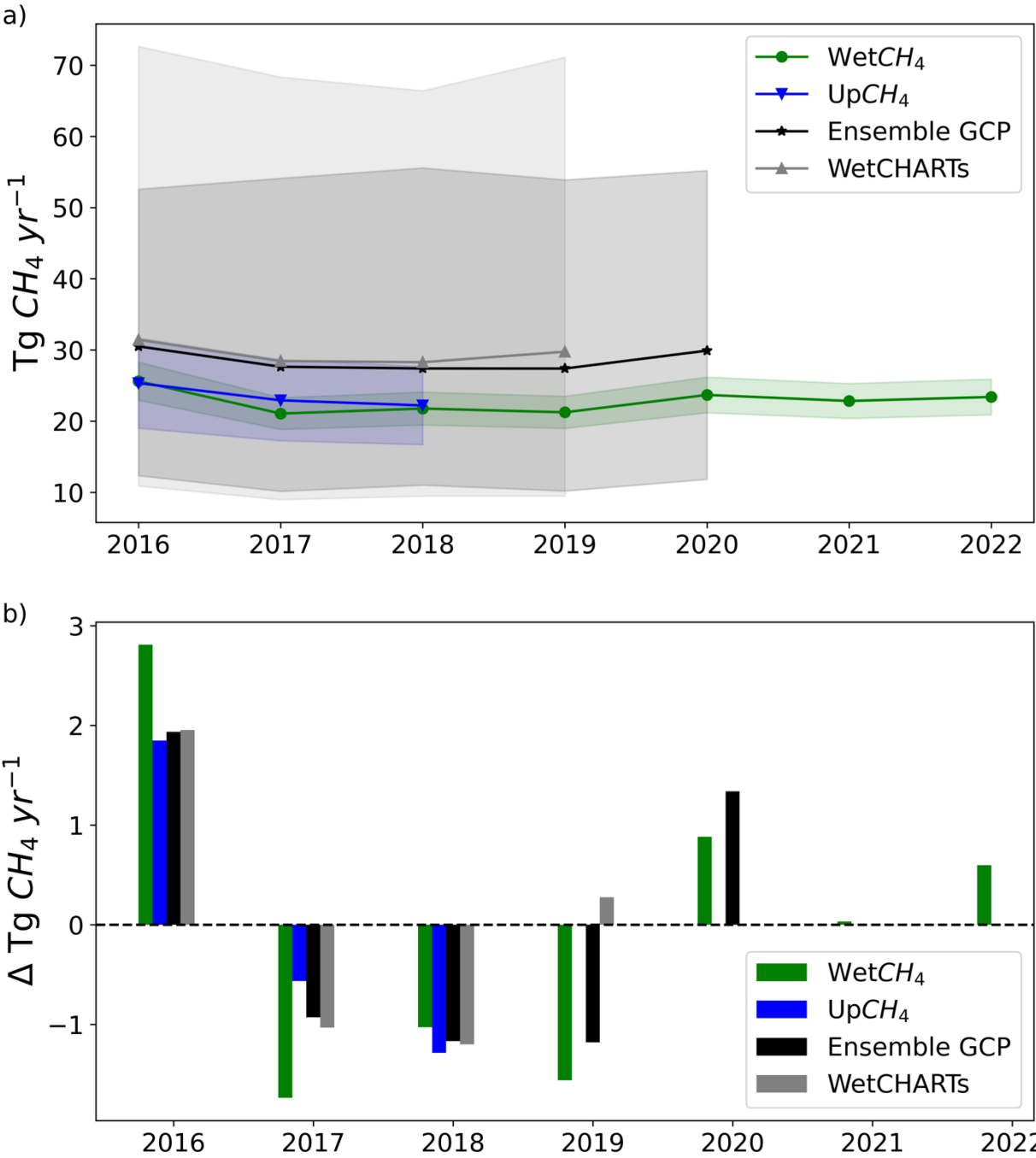
738
739 Fig. 8 Wetland CH_4 a) annual emissions and associated uncertainties in colored shades and b)
740 variations relative to multi-year means in the research domain (45° - 90° N). Wetland area data
741 applied in WetCH4 and UpCH4 was WAD2Mv2. Time periods of multi-year means: WetCH4
742 (2016-2022); UpCH4 (2016-2018); Ensemble GCP (2016-2020); WetCHARTs (2016-2019).
743
744 Subregional annual emissions and interannual variability (Fig. 9) of WetCH4 were calculated for
745 eight subregions in the northern high latitudes (Fig. S11): Siberian tundra, East Siberia, West

746 Siberia, Fennoscandia, Canadian tundra, East Canada, West Canada, and Alaska. The main
747 differences in WetCH$_4$ estimated emissions between WAD2Mv2 and GLWDv1 occurred in the
748 East Siberia, East Canada, West Canada, and Alaska subregions. However, interannual
749 variabilities were similar. Interannual variations from West Siberia accounted for 51% the
750 variations in domain emissions (Fig. 9a). The positive change in East Canada canceled the
751 negative change in West Siberia in 2021, resulting in low variability in the domain emission for
752 that year (Fig. 8). The relative interannual variability, which was calculated as the percentage of
753 a subregional variation to its period mean, was attributed to those from West Siberia,
754 Fennoscandia, West Canada, and Alaska (Fig. 9b).
755
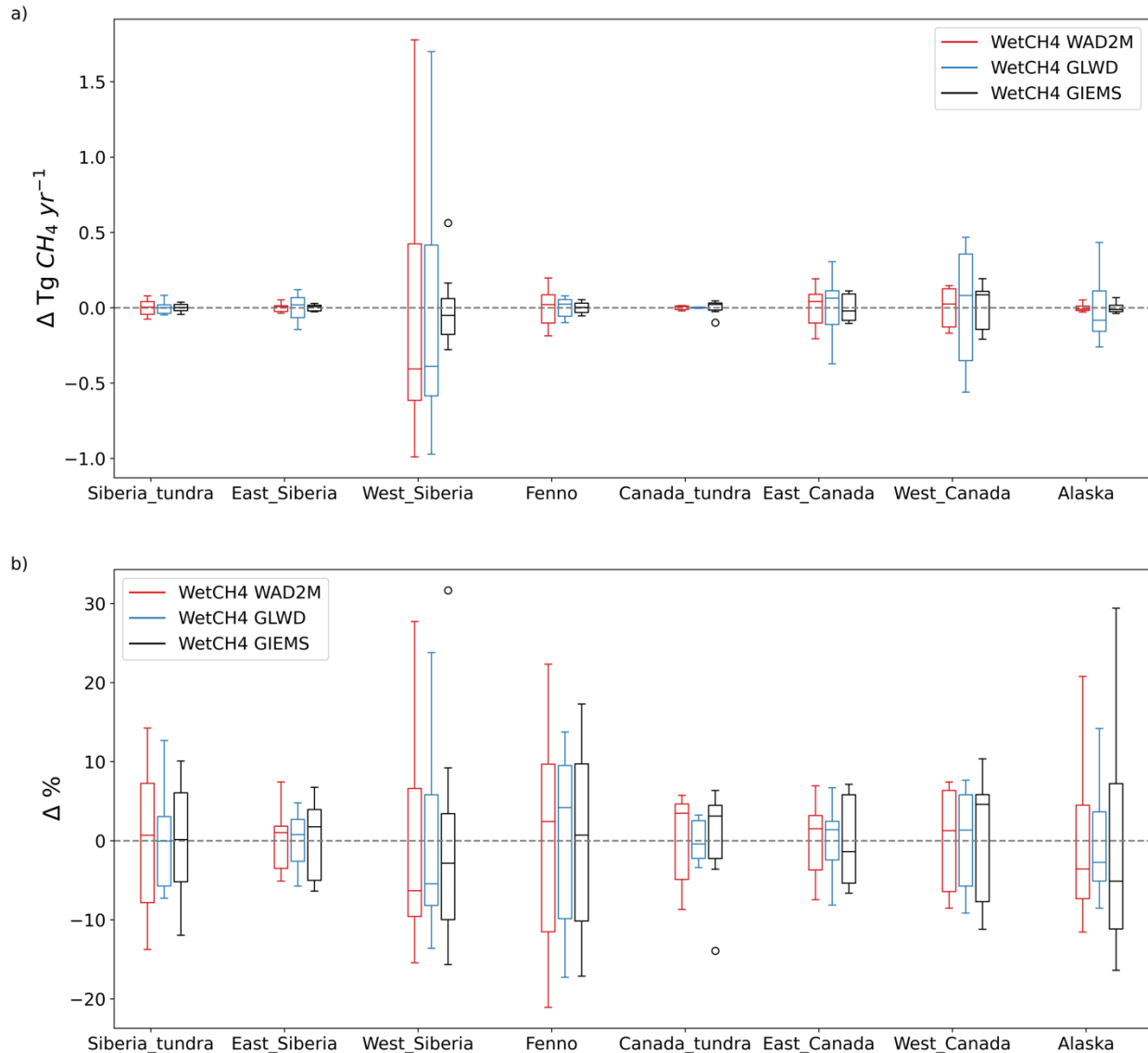
756
757 Fig. 9 Interannual variations and variability in subregions predicted by WetCH$_4$ with WAD2Mv2,
758 GLWDv1, and GIEMS2, respectively: (a) interannual variations with respect to period means
759 (2016-2022); (b) relative variability as the percentage of its period mean. Delta in the y axis
760 denotes the annual emissions minus mean annual emissions in the period 2016-2022. The

761 boxplots show the first quartile, the median, and the third quartile of the data with the whiskers
762 denoting the 1.5x interquartile range below/above the first/third quartile.

763 # 4. Discussion

764 This study provides new estimates of daily scale 10-km wetland CH_4 fluxes for the northern
765 terrestrial wetland region, upscaled from EC data. The upscaling framework was driven by
766 MERRA2 meteorological variables and soil temperatures and constrained by satellite products
767 from SMAP soil moisture and MODIS NBAR, resulting in a good prediction accuracy (mean R^2 =
768 0.70 and mean MAE =27 nmol m^{-2} s^{-1}) in monthly mean fluxes. Model agreement worsened at
769 daily and weekly timesteps due to higher variability in CH_4 fluxes at finer temporal resolutions. In
770 our framework, we applied a rigorous criterion on the counts of half-hourly observations to
771 control the selection quality of daily gap-filled data, which may filter out errors introduced by the
772 gap-filling process or lack of observations for calculating daily means. The improvement in
773 model performance can be partly attributed to the inclusion of soil temperature, satellite
774 assimilation of soil moisture, and MODIS vegetation reflectance in the framework that
775 represents controlling factors or proxies of CH_4 fluxes recognized in field experiments and
776 synthesis studies (Fig. 3).
777

778 ## 4.1 Important drivers to improve RF model predictive performance

779 Soil temperature plays an important role in microbial growth and dormancy (Chadburn et al.,
780 2020), and exponentially affects microbial CH_4 emission rates although the temperature
781 sensitivity varies across space and time (Knox et al., 2021; van Hulzen et al., 1999). In northern
782 wetlands, soil temperature is often more spatially variable relative to air temperature due to
783 snow insulation and active layer depth (Smith et al., 2022; W. Wang et al., 2016; Yuan et al.,
784 2022), and thus should be considered in upscaling models. Compared to air temperature or land
785 surface temperature that were used in previous upscaling studies (Peltola et al., 2019; McNicol
786 et al., 2023), the inclusion of MERRA2 soil temperatures in WetCH4 likely contributed to a higher
787 model predictive performance, although the impact of scale mismatch between the native
788 MERRA2 spatial resolution and the local footprints on the upscaled fluxes were not quantified.
789 Independent validation studies found significant correlations in the temporal trend and seasonal
790 cycles between MERRA2 soil temperatures and *in situ* observations (M. Li et al., 2020; Ma et
791 al., 2021) in the U.S. and mid-latitude Eurasia. However, lower correlations and overestimated
792 monthly variability were found in the cold season in Pan-Arctic (Herrington et al., 2022). This
793 suggests the impact of the uncertainty in MERRA2 soil temperatures were concentrated in the
794 cold season, when CH_4 fluxes were low. The agreement between ensemble means of soil
795 temperatures from eight reanalysis and land data assimilation system products and station
796 measurements improved in the pan-Arctic region (Herrington et al., 2022), suggesting the
797 potential to reduce upscaling uncertainty forced by the ensemble mean of reanalysis datasets.
798

799   Emergent vegetation with aerenchyma affects the recent substrate availability and the plant-
800   mediated transport of CH_4 (Kyzivat et al., 2022; Melack & Hess, 2023). We used the full land
801   bands of the MODIS NBAR product rather than derived vegetation indices used in previous
802   upscaling studies, as signals indicating wetland vegetation functional characteristics may be lost
803   when merging bands to derive simple vegetation indices (Chen et al., 2013). In our study, the
804   near-infrared and shortwave infrared bands (NBAR bands 2, 5, and 7) presented relatively high
805   importance in the RF model due to their associations with vegetation characteristics and water
806   table dynamics in northern peatlands (Baskaran et al., 2022; Burdun et al., 2023). Satellite
807   inputs provide high spatial resolution constraints on the environmental variability and help
808   reduce model spatial predictive errors (Fig. 3), indicating the requirement of high spatial
809   resolution driving input for accurately modeling wetland CH_4 fluxes (Elder et al., 2021).
810
811   Surface and rootzone soil moisture are important controls on ecosystem anaerobic metabolism.
812   Low soil moisture implies oxic conditions and allows methanotrophic bacteria to consume CH_4,
813   whereas high soil moisture enables CH_4 production and suppresses consumption (Liebner et
814   al., 2011; Olefeldt et al., 2013; Spahni et al., 2011). Soil wetness estimated in the rootzone and
815   the profile from SMAP measurements may be able to capture water table dynamics and hence
816   ranked as important in WetCH4 model performance. Validation of the SMAP level 4 soil moisture
817   data assimilation product has shown that it meets the performance requirement of unbiased
818   root-mean-square error <0.04 m^3/m^3 (Colliander et al., 2022). However, the validation sites are
819   mostly located in North American grassland, cropland and shrubland, requiring more *in situ* soil
820   moisture observations in high latitude tundra and peatland. Regional validation studies
821   suggested uncertainties of satellite derived soil moisture including SMAP at high latitudes were
822   high (Högström et al., 2018; Wrona et al., 2017) and remained to be addressed.
823
824   Underground processes of CH_4 production and oxidation are difficult to model (Ueyama, Knox,
825   et al., 2023), especially for seasonal cycles in the northern high latitudes. A hysteresis effect
826   that manifests intra-seasonal variability in the dependence of CH_4 fluxes on temperature has
827   been observed at EC sites (K.-Y. Chang et al., 2021), but it was not reproduced in WetCH4.
828   Positive hysteresis and the difference in frozen status from topsoil to deep soil during autumn
829   freeze results in zero curtain periods that have been observed at high latitude tundra (Bao et al.,
830   2021; Zona et al., 2016), the occurrence of which was subsequently underestimated in our
831   model.
832
833   The amount of additional substrate available for methanogenesis due to soil freezing/thawing,
834   missing in our framework, could be a controlling factor of the occurrence of this phenomenon.
835   Higher substrate availability elevates methanogen abundance and activities during autumn
836   freeze (Bao et al., 2021). However, spatially explicit substrate data are not available. Using
837   proxies such as net primary production or EVI for substrate availability might be oversimplified
838   (Larmola et al., 2010; T. Li et al., 2016; Peltola et al., 2019). In addition, the uncertainty of deep
839   soil temperature of training inputs in late autumn may hinder the model's ability to capture
840   patterns of high emissions during zero curtain periods observed at Alaska tundra (Fig. S10).
841   More temporally accurate soil temperature data is needed to delineate the soil freezing progress
842   and properly constrain predictions of CH_4 emission during the cold season (Arndt et al., 2019).

843   The UpCH$_4$ results (McNicol et al., 2023) also suggest that simply imposing lags to temporal
844   predictors in RF cannot capture complex intra-seasonal variability due to the complicated lag
845   effects interacting with the water table depth (Turner et al., 2021). Without timestamps in
846   predictors, RF treats time series fluxes independently, which may limit its predictive
847   performance. Deep learning models designed to account for temporal progress in data, such as
848   Long Short Term Memory (LSTM) neural networks, may improve modeling accuracy of
849   seasonal cycles (Reichstein et al., 2019; Yuan et al., 2022).
850

851   4.2 Data limitations in current EC CH$_4$ observations

852   Data deficiency in EC CH$_4$ flux observations in winter and in under-represented areas limited the
853   RF model's extrapolation ability. Data abundance and representativeness across space, time,
854   and wetland types drives model performance and ability to extrapolate for the data-driven
855   approach. The 26 wetland EC sites included in this study are largely located in Fennoscandia,
856   East Canada and Alaska (Fig. 2), leaving some regional emission hotspots under-represented.
857   For instance, Western Siberian Lowlands, the large wetland complex and the major contributor
858   of interannual variations of CH$_4$ in the region, has limited data that is compiled from a single site
859   (RU-VRK, not included in this study due to the observations before our study period). Cold
860   season emissions could contribute a substantial fraction of the Arctic tundra annual CH$_4$ budget
861   (Mastepanov et al., 2008; Mavrovic et al., 2024; Zona et al., 2016). But after filtering, 23% of the
862   EC data in high latitudes (>60° N) were recorded between November and March, which could
863   be insufficient for accurately modeling and upscaling zero curtain period fluxes.
864

865   Ten bog and fen sites used for modeling contain all season daily flux records with more than 11
866   half-hourly observations per day, all from Fennoscandia and Canada. Although Alaska is
867   represented by 11 wetland sites, sufficient winter observations with good quality are still
868   needed. West Siberian Lowlands are underrepresented by EC CH$_4$ sites. Missing data in
869   MODIS NBAR due to snow cover or gaps in SMAP reduced training data by 31% and 48% in
870   the study domain, respectively. Filling data of MODIS NBAR to account for snow cover
871   information and gap-filling SMAP soil moisture products can make full use of available EC
872   observations and help improve model performance in cold seasons. Since gaps in winter SMAP
873   data were filled with zero values, our approach has limitations in the estimation in winter soil
874   moisture gaps in areas where zero curtain and talik were not represented by our interpolated
875   soil temperatures, for example, in coastal areas.
876

877   Many wetland sites in the study are located in areas with peatland presence, with 35% of sites
878   in peatland-rich areas with >50% peatland cover (Hugelius et al., 2020). Mineral soil (soil
879   containing less than 12% organic carbon by weight) marshes, though covering only 5% of the
880   total wetland area in the northern high latitudes, need to be considered when deploying new EC
881   sites due to their high CH$_4$ emissions (Kuhn et al., 2021; Olefeldt et al., 2021). This study
882   identified regional CH$_4$ emission hotspots and areas undergoing strong interannual variations,
883   which are yet not part of the current FLUXNET network. However, the 10 km resolution of the
884   RF estimates prohibits the identification of local hotspots that may occur at <1-10 m scales

885 (Elder et al., 2021). The wall-to-wall flux maps also provide spatially continuous information for
886 effectively further developing the CH_4 flux tower network.
887

888 4.3 Budget comparison

889 WetCH$_4$ estimated annual and seasonal mean emissions that were comparable to existing data-
890 driven products in the study domain (Table S3). With the dynamic WAD2Mv2 map, our
891 estimation was 0.7 Tg CH$_4$ yr^{-1} smaller than UpCH$_4$ due to the mean seasonal cycles between
892 2010 and 2020 from WAD2M applied in our estimation. With the same static GLWDv1 map, our
893 estimation was about 22% larger than the estimate from Peltola et al. (37.5 ±12 Tg CH$_4$ yr^{-1} for
894 2013-2014) despite the different periods. This is attributed to higher fluxes estimated by WetCH$_4$
895 in DJF and JJA seasons. With two versions of the static GLWD maps, we estimated potential
896 annual emissions between 46.0 and 51.6 Tg CH$_4$ yr^{-1}. Compared to GLWDv1, version 2 of
897 GLWD mapped smaller wetland fractions in the Hudson Bay Lowlands with intense CH$_4$ fluxes
898 and more wetlands in the northwest of the Ural Mountains, Eastern Siberia, and the Sanjiang
899 Plain, where CH$_4$ intensities were weaker, resulting in a larger estimate of the annual emission
900 (Fig. S13). The wide range of data-driven estimates was driven by the differences in wetland
901 maps. While WAD2M provides crucial information on wetland inundation dynamics controlling
902 interannual and inter-seasonal changes in CH$_4$ emitting areas, areas with saturated soil in the
903 Arctic tundra are likely severely underestimated (Fig. 8d), requiring more accurate maps
904 delineating wet tundra communities at higher spatial resolution (e.g., < 1 km). Incorporating
905 wetland fractions derived from high-resolution thematic maps (e.g., CALU) can improve the use
906 of WAD2M in cold regions. Developing/improving higher resolution microwave remote sensing
907 products capable of tracking dynamic changes in local soil moisture conditions is also needed.
908 Together, these two components likely currently yield the largest sources of uncertainty in high
909 latitude terrestrial CH$_4$ budgets.
910

911 Bottom-up estimates on wetland CH$_4$ emissions from data-driven, GCP ensemble means and
912 WetCHARTs are smaller than the top-down CarbonTracker-CH$_4$ estimate on natural microbial
913 emissions because the latter includes emissions from aquatic systems. Aquatic CH$_4$ emissions
914 for this region have been estimated at 5.5 Tg CH$_4$ yr^{-1} from rivers and streams (Rocher-Ros et
915 al., 2023) and 16.6 Tg CH$_4$ yr^{-1} from lakes (Johnson et al., 2022). The total emissions budget for
916 wetlands and open water, based on this study and the aquatic estimates, are about 44.9 Tg CH$_4$
917 yr^{-1}, which is 4 Tg CH$_4$ yr^{-1} more than the CarbonTracker-CH$_4$ estimate. The amplitudes of
918 WetCH$_4$ seasonal mean fluxes align with bottom up and top down estimates. Differences in the
919 seasonal dynamics of wetland maps are the major source of upscaling uncertainty and result in
920 various uncertainties between regional estimates. While atmospheric inversion models need
921 bottom-up estimates as priors, data-driven upscaled CH$_4$ products offer alternatives to process-
922 based estimates to assist with inversion models in regions where data-driven models perform
923 well (Bloom et al., 2017; Melton et al., 2013).
924

4.4 Future directions

Future development of EC networks in the northern high latitudes is urgently needed to provide additional observations needed to improve model-based upscaling of CH_4 flux budgets, and to address current gaps in ecosystem and regional representation. Deploying new sites in under-represented areas will not only benefit flux upscaling efforts but also our understanding of how ecosystem metabolism responds to the changing climate (Baldocchi, 2020; Pallandt et al., 2022; Villarreal & Vargas, 2021). With the availability of long-term predictor variable data, it is possible to expand upscaling frameworks over longer periods (e.g., 2000 to current), when adequate flux observations in 2000-2010 from chambers are compiled, as 96% of the data were recorded after 2010 in FLUXNET-CH_4 (McNicol et al., 2023).

Several data products exist for the meteorological predictor variables. Quantifying measurement uncertainties between products of predictor variables and how the uncertainties propagate to upscaling products need to be addressed in future work. The mismatch of spatial scales between tower footprints and predictor variables may cause underestimation of abruptly high fluxes measured at tower landscapes when environmental conditions are averaged over half-degree grids (Chu et al., 2021; McNicol et al., 2023). Therefore, downscaling predictor variables for developing higher-resolution products is needed, especially for the Arctic region where thermokarst development is shaping permafrost landscapes with fragments of wetlands, thermokarst ponds, and forests (Miner et al., 2022; Osterkamp et al., 2000; Wik et al., 2016). For example, Fang et al. (2022) have downscaled global SMAP surface soil moisture to 1-km resolution, and Optical/Thermal and microwave fusion methods have been developed to downscale soil moisture (J. Peng et al., 2017). Nevertheless, downscaled products for rootzone or profile soil moisture are needed for upscaling CH_4 fluxes as are soil temperature products.

Beyond the ML-based upscaling framework, hybrid modeling of the data-driven approach and process-based models is a promising but also challenging direction of future study (Reichstein et al., 2019). One practice constrained regional data-driven fluxes with top-down estimates via auto-learned weights on per pixel fluxes in a region (Upton et al., 2023). Another practice pretrained a time-dependent ML algorithm with initialization from process-based synthetic data and then fine-tuned the model with observations (Liu et al., 2022). Finally, leveraging physical constraints to increase the interpretability of data-driven models and computation efficiency is still an important factor to consider in all hybrid modeling.

5. Code and data availability

The daily CH_4 flux intensities in the northern wetlands at a spatial resolution of 0.098° x 0.098°and associated uncertainties, along with daily emissions weighted by WAD2M, GIEMS2, and GLWDv1, can be accessed through https://doi.org/10.5281/zenodo.10802153 (Ying et al., 2024). Source code of ML modeling and upscaling is publicly available at https://github.com/qlearwater/WetCH4.git. Half-hourly EC data is available for download at https://fluxnet.org/data/fluxnet-ch4-community-product/ (Delwiche et al., 2021).

6. Conclusions

We developed an ML framework (WetCH$_4$) to upscale daily wetland CH$_4$ fluxes of mid-high northern latitudes at 10-km spatial resolution combining EC tower measurements with satellite observations and climate reanalysis. WetCH$_4$ is novel in that it is the first upscaling framework to introduce SMAP soil moisture and MODIS reflectance in modeling wetland CH$_4$ fluxes to improve accuracy (mean R^2 = 0.70). The remote-sensing products provided high spatial resolution constraints associated with the abiotic controllers of CH$_4$ fluxes, indicating the importance of using high spatial resolution inputs in models for accurately simulating the spatiotemporally variable CH$_4$ emissions from heterogeneous northern wetland landscapes. The framework highlights the importance of soil temperature, vegetation, and soil moisture for modeling CH$_4$ fluxes in a data-driven approach. Using WetCH$_4$, an average annual CH$_4$ emissions of 22.8 ±2.4 Tg CH$_4$ yr^{-1} with WAD2Mv2 was estimated and ranged between 15.7 ±1.8 Tg CH$_4$ yr^{-1} with GIEMS2 and 51.6 ±2.2 Tg CH$_4$ yr^{-1} with GLWDv2 from vegetated wetlands (>45° N) for 2016-2022, approximately 14-32% of the global wetland CH$_4$ budget (Saunois et al., 2020). Differences in estimates of wetland CH$_4$ emissions due to different wetland maps applied, highlighting the need for high resolution wetland maps and accurate delineation of wet soil dynamics. Emissions were relatively lower in 2017-2019 and intensified in 2016, 2020 and 2022, with the largest interannual variations coming from West Siberia. Spatio-temporal distributions of CH$_4$ fluxes find emission hotspots and regions of intensified interannual variations that are not currently measured with EC. Comparing with current EC sites, we suggest a need for tower observations in wetlands of West Siberia and West Canada and diversified observations across wetland types. More site observations in soil water related variables are needed for improved understanding of flux controls in northern wetland ecosystems. Future wetland CH$_4$ upscaling work could benefit from improved soil moisture products and hybrid modeling.

Acknowledgements

This work was supported by funding catalyzed by the TED Audacious Project (Permafrost Pathways). Resources supporting this work were provided by the NASA High-End Computing (HEC) Program through the NASA Center for Climate Simulation (NCCS) at Goddard Space Flight Center. We thank Sara Knox and Gavin McNicol for their helpful suggestions in the early stages of the compilation of EC CH$_4$ fluxes and the development of the upscaling product, respectively. Ben Poulter acknowledges support from the NASA Terrestrial Ecology Program. Annett Bartsch was supported by the European Space Agency CCI+ Permafrost and AMPAC-Net projects. Aram Kalhori was supported by the European Union's Horizon Europe program, grant agreement no. 101056848.

References

Alonso, A., Muñoz-Carpena, R., & Kaplan, D. (2020). Coupling high-resolution field monitoring and MODIS for reconstructing wetland historical hydroperiod at a high temporal frequency. *Remote Sensing of Environment*, *247*, 111807. https://doi.org/10.1016/j.rse.2020.111807

Amatulli, G., McInerney, D., Sethi, T., Strobl, P., & Domisch, S. (2020). Geomorpho90m, empirical evaluation and accuracy assessment of global high-resolution geomorphometric layers. *Scientific Data*, *7*(1), Article 1. https://doi.org/10.1038/s41597-020-0479-6

Arndt, K. A., Oechel, W. C., Goodrich, J. P., Bailey, B. A., Kalhori, A., Hashemi, J., Sweeney, C., & Zona, D. (2019). Sensitivity of Methane Emissions to Later Soil Freezing in Arctic Tundra Ecosystems. *Journal of Geophysical Research: Biogeosciences*, *124*(8), 2595–2609. https://doi.org/10.1029/2019JG005242

Avis, C. A., Weaver, A. J., & Meissner, K. J. (2011). Reduction in areal extent of high-latitude wetlands in response to permafrost thaw. *Nature Geoscience*, *4*(7), 444–448. https://doi.org/10.1038/ngeo1160

Aydin, M., Verhulst, K. R., Saltzman, E. S., Battle, M. O., Montzka, S. A., Blake, D. R., Tang, Q., & Prather, M. J. (2011). Recent decreases in fossil-fuel emissions of ethane and methane derived from firn air. *Nature*, *476*(7359), Article 7359. https://doi.org/10.1038/nature10352

Baldocchi, D. D. (2003). Assessing the eddy covariance technique for evaluating carbon dioxide exchange rates of ecosystems: Past, present and future. *Global Change Biology*, *9*(4), 479–492. https://doi.org/10.1046/j.1365-2486.2003.00629.x

Baldocchi, D. D. (2020). How eddy covariance flux measurements have contributed to our understanding of Global Change Biology. *Global Change Biology*, *26*(1), 242–260. https://doi.org/10.1111/gcb.14807

Bansal, S., Creed, I. F., Tangen, B. A., Bridgham, S. D., Desai, A. R., Krauss, K. W., Neubauer, S. C., Noe, G. B., Rosenberry, D. O., Trettin, C., Wickland, K. P., Allen, S. T., Arias-Ortiz, A., Armitage, A. R., Baldocchi, D., Banerjee, K., Bastviken, D., Berg, P., Bogard, M. J., … Zhu, X. (2023). Practical Guide to Measuring Wetland Carbon Pools and Fluxes. *Wetlands*, *43*(8), 105. https://doi.org/10.1007/s13157-023-01722-2

Bao, T., Xu, X., Jia, G., Billesbach, D. P., & Sullivan, R. C. (2021). Much stronger tundra methane emissions during autumn freeze than spring thaw. *Global Change Biology*, *27*(2), 376–387. https://doi.org/10.1111/gcb.15421

Baray, S., Jacob, D. J., Maasakkers, J. D., Sheng, J.-X., Sulprizio, M. P., Jones, D. B. A., Bloom, A. A., & McLaren, R. (2021). Estimating 2010–2015 anthropogenic and natural methane emissions in Canada using ECCC surface and GOSAT satellite observations. *Atmospheric Chemistry and Physics*, *21*(23), 18101–18121. https://doi.org/10.5194/acp-21-18101-2021

Bartsch, A., Efimova, A., Widhalm, B., Muri, X., von Baeckmann, C., Bergstedt, H., Ermokhina, K., Hugelius, G., Heim, B., & Leibman, M. (2024). Circumarctic land cover diversity considering wetness gradients. *Hydrology and Earth System Sciences*, *28*(11), 2421–2481. https://doi.org/10.5194/hess-28-2421-2024

Baskaran, L., Elder, C., Bloom, A. A., Ma, S., Thompson, D., & Miller, C. E. (2022).
Geomorphological patterns of remotely sensed methane hot spots in the Mackenzie
Delta, Canada. *Environmental Research Letters*, *17*(1), 015009.
https://doi.org/10.1088/1748-9326/ac41fb

Beaulieu, J. J., Waldo, S., Balz, D. A., Barnett, W., Hall, A., Platz, M. C., & White, K. M. (2020).
Methane and Carbon Dioxide Emissions From Reservoirs: Controls and Upscaling.
Journal of Geophysical Research: Biogeosciences, *125*(12), e2019JG005474.
https://doi.org/10.1029/2019JG005474

Bergamaschi, P., Houweling, S., Segers, A., Krol, M., Frankenberg, C., Scheepmaker, R. A.,
Dlugokencky, E., Wofsy, S. C., Kort, E. A., Sweeney, C., Schuck, T., Brenninkmeijer, C.,
Chen, H., Beck, V., & Gerbig, C. (2013). Atmospheric CH4 in the first decade of the 21st
century: Inverse modeling analysis using SCIAMACHY satellite retrievals and NOAA
surface measurements. *Journal of Geophysical Research: Atmospheres*, *118*(13), 7350–
7369. https://doi.org/10.1002/jgrd.50480

Bloom, A. A., Bowman, K. W., Lee, M., Turner, A. J., Schroeder, R., Worden, J. R., Weidner, R.,
McDonald, K. C., & Jacob, D. J. (2017). A global wetland methane emissions and
uncertainty dataset for atmospheric chemical transport models (WetCHARTs version
1.0). *Geoscientific Model Development*, *10*(6), 2141–2156. https://doi.org/10.5194/gmd-
10-2141-2017

Bloom, A. A., Palmer, P. I., Fraser, A., Reay, D. S., & Frankenberg, C. (2010). Large-Scale
Controls of Methanogenesis Inferred from Methane and Gravity Spaceborne Data.
Science, *327*(5963), 322–325. https://doi.org/10.1126/science.1175176

Bodesheim, P., Jung, M., Gans, F., Mahecha, M. D., & Reichstein, M. (2018). Upscaled diurnal
cycles of land–atmosphere fluxes: A new global half-hourly data product. *Earth System
Science Data*, *10*(3), 1327–1365. https://doi.org/10.5194/essd-10-1327-2018

Breiman, L. (2001). Random Forests. *Machine Learning*, *45*(1), 5–32.
https://doi.org/10.1023/A:1010933404324

Bruhwiler, L., Dlugokencky, E., Masarie, K., Ishizawa, M., Andrews, A., Miller, J., Sweeney, C.,
Tans, P., & Worthy, D. (2014). CarbonTracker-CH4: An assimilation system for
estimating emissions of atmospheric methane. *Atmospheric Chemistry and Physics*,
14(16), 8269–8293. https://doi.org/10.5194/acp-14-8269-2014

Burdun, I., Bechtold, M., Aurela, M., De Lannoy, G., Desai, A. R., Humphreys, E., Kareksela, S.,
Komisarenko, V., Liimatainen, M., Marttila, H., Minkkinen, K., Nilsson, M. B., Ojanen, P.,
Salko, S.-S., Tuittila, E.-S., Uuemaa, E., & Rautiainen, M. (2023). Hidden becomes
clear: Optical remote sensing of vegetation reveals water table dynamics in northern
peatlands. *Remote Sensing of Environment*, *296*, 113736.
https://doi.org/10.1016/j.rse.2023.113736

Chadburn, S. E., Aalto, T., Aurela, M., Baldocchi, D., Biasi, C., Boike, J., Burke, E. J., Comyn-
Platt, E., Dolman, A. J., Duran-Rojas, C., Fan, Y., Friborg, T., Gao, Y., Gedney, N.,
Göckede, M., Hayman, G. D., Holl, D., Hugelius, G., Kutzbach, L., … Westermann, S.
(2020). Modeled Microbial Dynamics Explain the Apparent Temperature Sensitivity of
Wetland Methane Emissions. *Global Biogeochemical Cycles*, *34*(11), e2020GB006678.
https://doi.org/10.1029/2020GB006678

Chang, K.-Y., Riley, W. J., Knox, S. H., Jackson, R. B., McNicol, G., Poulter, B., Aurela, M.,
  Baldocchi, D., Bansal, S., Bohrer, G., Campbell, D. I., Cescatti, A., Chu, H., Delwiche, K.
  B., Desai, A. R., Euskirchen, E., Friborg, T., Goeckede, M., Helbig, M., … Zona, D.
  (2021). Substantial hysteresis in emergent temperature sensitivity of global wetland CH4
  emissions. *Nature Communications*, *12*(1), Article 1. https://doi.org/10.1038/s41467-021-
  22452-1

Chang, R. Y.-W., Miller, C. E., Dinardo, S. J., Karion, A., Sweeney, C., Daube, B. C.,
  Henderson, J. M., Mountain, M. E., Eluszkiewicz, J., Miller, J. B., Bruhwiler, L. M. P., &
  Wofsy, S. C. (2014). Methane emissions from Alaska in 2012 from CARVE airborne
  observations. *Proceedings of the National Academy of Sciences*, *111*(47), 16694–
  16699. https://doi.org/10.1073/pnas.1412953111

Chen, Y., Huang, C., Ticehurst, C., Merrin, L., & Thew, P. (2013). An Evaluation of MODIS Daily
  and 8-day Composite Products for Floodplain and Wetland Inundation Mapping.
  Wetlands, *33*(5), 823–835. https://doi.org/10.1007/s13157-013-0439-4

Choe, H., Chi, J., & Thorne, J. H. (2021). Mapping Potential Plant Species Richness over Large
  Areas with Deep Learning, MODIS, and Species Distribution Models. *Remote Sensing*,
  13(13), Article 13. https://doi.org/10.3390/rs13132490

Chu, H., Luo, X., Ouyang, Z., Chan, W. S., Dengel, S., Biraud, S. C., Torn, M. S., Metzger, S.,
  Kumar, J., Arain, M. A., Arkebauer, T. J., Baldocchi, D., Bernacchi, C., Billesbach, D.,
  Black, T. A., Blanken, P. D., Bohrer, G., Bracho, R., Brown, S., … Zona, D. (2021).
  Representativeness of Eddy-Covariance flux footprints for areas surrounding AmeriFlux
  sites. *Agricultural and Forest Meteorology*, *301–302*, 108350.
  https://doi.org/10.1016/j.agrformet.2021.108350

Colliander, A., Reichle, R. H., Crow, W. T., Cosh, M. H., Chen, F., Chan, S., Das, N. N.,
  Bindlish, R., Chaubell, J., Kim, S., Liu, Q., O'Neill, P. E., Dunbar, R. S., Dang, L. B.,
  Kimball, J. S., Jackson, T. J., Al-Jassar, H. K., Asanuma, J., Bhattacharya, B. K., …
  Yueh, S. H. (2022). Validation of Soil Moisture Data Products From the NASA SMAP
  Mission. *IEEE Journal of Selected Topics in Applied Earth Observations and Remote
  Sensing*, *15*, 364–392. https://doi.org/10.1109/JSTARS.2021.3124743

Davidson, S. J., Santos, M. J., Sloan, V. L., Reuss-Schmidt, K., Phoenix, G. K., Oechel, W. C.,
  & Zona, D. (2017). Upscaling CH4 Fluxes Using High-Resolution Imagery in Arctic
  Tundra Ecosystems. *Remote Sensing*, *9*(12), Article 12.
  https://doi.org/10.3390/rs9121227

Delwiche, K. B., Knox, S. H., Malhotra, A., Fluet-Chouinard, E., McNicol, G., Feron, S., Ouyang,
  Z., Papale, D., Trotta, C., Canfora, E., Cheah, Y.-W., Christianson, D., Alberto, M. C. R.,
  Alekseychik, P., Aurela, M., Baldocchi, D., Bansal, S., Billesbach, D. P., Bohrer, G., …
  Jackson, R. B. (2021). FLUXNET-CH$_4$: A global, multi-ecosystem dataset and analysis
  of methane seasonality from freshwater wetlands. *Earth System Science Data*, *13*(7),
  3607–3689. https://doi.org/10.5194/essd-13-3607-2021

Elder, C. D., Thompson, D. R., Thorpe, A. K., Chandanpurkar, H. A., Hanke, P. J., Hasson, N.,
  James, S. R., Minsley, B. J., Pastick, N. J., Olefeldt, D., Walter Anthony, K. M., & Miller,
  C. E. (2021). Characterizing Methane Emission Hotspots From Thawing Permafrost.
  Global Biogeochemical Cycles, *35*(12), e2020GB006922.
  https://doi.org/10.1029/2020GB006922

Entekhabi, D., Njoku, E. G., O'Neill, P. E., Kellogg, K. H., Crow, W. T., Edelstein, W. N., Entin, J. K., Goodman, S. D., Jackson, T. J., Johnson, J., Kimball, J., Piepmeier, J. R., Koster, R. D., Martin, N., McDonald, K. C., Moghaddam, M., Moran, S., Reichle, R., Shi, J. C., … Van Zyl, J. (2010). The Soil Moisture Active Passive (SMAP) Mission. *Proceedings of the IEEE*, *98*(5), 704–716. https://doi.org/10.1109/JPROC.2010.2043918

Euskirchen, E. S., Edgar, C. W., Kane, E. S., Waldrop, M. P., Neumann, R. B., Manies, K. L., Douglas, T. A., Dieleman, C., Jones, M. C., & Turetsky, M. R. (2024). Persistent net release of carbon dioxide and methane from an Alaskan lowland boreal peatland complex. *Global Change Biology*, *30*(1), e17139. https://doi.org/10.1111/gcb.17139

Fang, B., Lakshmi, V., Cosh, M., Liu, P.-W., Bindlish, R., & Jackson, T. J. (2022). A global 1-km downscaled SMAP soil moisture product based on thermal inertia theory. *Vadose Zone Journal*, *21*(2), e20182. https://doi.org/10.1002/vzj2.20182

Feron, S., Malhotra, A., Bansal, S., Fluet-Chouinard, E., McNicol, G., Knox, S. H., Delwiche, K. B., Cordero, R. R., Ouyang, Z., Zhang, Z., Poulter, B., & Jackson, R. B. (2024). Recent increases in annual, seasonal, and extreme methane fluxes driven by changes in climate and vegetation in boreal and temperate wetland ecosystems. *Global Change Biology*, *30*(1), e17131. https://doi.org/10.1111/gcb.17131

Friedlingstein, P., Jones, M. W., O'Sullivan, M., Andrew, R. M., Bakker, D. C. E., Hauck, J., Le Quéré, C., Peters, G. P., Peters, W., Pongratz, J., Sitch, S., Canadell, J. G., Ciais, P., Jackson, R. B., Alin, S. R., Anthoni, P., Bates, N. R., Becker, M., Bellouin, N., … Zeng, J. (2022). Global Carbon Budget 2021. *Earth System Science Data*, *14*(4), 1917–2005. https://doi.org/10.5194/essd-14-1917-2022

Gelaro, R., McCarty, W., Suárez, M. J., Todling, R., Molod, A., Takacs, L., Randles, C. A., Darmenov, A., Bosilovich, M. G., Reichle, R., Wargan, K., Coy, L., Cullather, R., Draper, C., Akella, S., Buchard, V., Conaty, A., Silva, A. M. da, Gu, W., … Zhao, B. (2017). The Modern-Era Retrospective Analysis for Research and Applications, Version 2 (MERRA-2). *Journal of Climate*, *30*(14), 5419–5454. https://doi.org/10.1175/JCLI-D-16-0758.1

Heimann, M. (2011). Enigma of the recent methane budget. *Nature*, *476*(7359), Article 7359. https://doi.org/10.1038/476157a

Herrington, T. C., Fletcher, C. G., & Kropp, H. (2022). Validation of Pan-Arctic Soil Temperatures in Modern Reanalysis and Data Assimilation Systems. *The Cryosphere Discussions*, 1–33. https://doi.org/10.5194/tc-2022-5

Högström, E., Heim, B., Bartsch, A., Bergstedt, H., & Pointner, G. (2018). Evaluation of a MetOp ASCAT-Derived Surface Soil Moisture Product in Tundra Environments. *Journal of Geophysical Research: Earth Surface*, *123*(12), 3190–3205. https://doi.org/10.1029/2018JF004658

Houborg, R., Soegaard, H., & Boegh, E. (2007). Combining vegetation index and model inversion methods for the extraction of key vegetation biophysical parameters using Terra and Aqua MODIS reflectance data. *Remote Sensing of Environment*, *106*(1), 39–58. https://doi.org/10.1016/j.rse.2006.07.016

Hugelius, G., Loisel, J., Chadburn, S., Jackson, R. B., Jones, M., MacDonald, G., Marushchak, M., Olefeldt, D., Packalen, M., Siewert, M. B., Treat, C., Turetsky, M., Voigt, C., & Yu, Z. (2020). Large stocks of peatland carbon and nitrogen are vulnerable to permafrost thaw.

1174   *Proceedings of the National Academy of Sciences*, *117*(34), 20438–20446.

1175   https://doi.org/10.1073/pnas.1916387117

1176 IPCC AR6. (2023). *AR6 Synthesis Report: Climate Change 2023 — IPCC*.

1177   https://www.ipcc.ch/report/sixth-assessment-report-cycle/

1178 Irvin, J., Zhou, S., McNicol, G., Lu, F., Liu, V., Fluet-Chouinard, E., Ouyang, Z., Knox, S. H.,

1179   Lucas-Moffat, A., Trotta, C., Papale, D., Vitale, D., Mammarella, I., Alekseychik, P.,

1180   Aurela, M., Avati, A., Baldocchi, D., Bansal, S., Bohrer, G., … Jackson, R. B. (2021).

1181   Gap-filling eddy covariance methane fluxes: Comparison of machine learning model

1182   predictions and uncertainties at FLUXNET-CH4 wetlands. *Agricultural and Forest*

1183   *Meteorology*, *308–309*, 108528. https://doi.org/10.1016/j.agrformet.2021.108528

1184 Iwata, H., Harazono, Y., Ueyama, M., Sakabe, A., Nagano, H., Kosugi, Y., Takahashi, K., &

1185   Kim, Y. (2015). Methane exchange in a poorly-drained black spruce forest over

1186   permafrost observed using the eddy covariance technique. *Agricultural and Forest*

1187   *Meteorology*, *214–215*, 157–168. https://doi.org/10.1016/j.agrformet.2015.08.252

1188 Jiao, M., Zhao, L., Wang, C., Hu, G., Li, Y., Zhao, J., Zou, D., Xing, Z., Qiao, Y., Liu, G., Du, E.,

1189   Xiao, M., & Hou, Y. (2023). Spatiotemporal Variations of Soil Temperature at 10 and 50

1190   cm Depths in Permafrost Regions along the Qinghai-Tibet Engineering Corridor. *Remote*

1191   *Sensing*, *15*(2), Article 2. https://doi.org/10.3390/rs15020455

1192 Johnson, M. S., Matthews, E., Bastviken, D., Deemer, B., Du, J., & Genovese, V. (2021).

1193   Spatiotemporal Methane Emission From Global Reservoirs. *Journal of Geophysical*

1194   *Research: Biogeosciences*, *126*(8), e2021JG006305.

1195   https://doi.org/10.1029/2021JG006305

1196 Johnson, M. S., Matthews, E., Du, J., Genovese, V., & Bastviken, D. (2022). Methane Emission

1197   From Global Lakes: New Spatiotemporal Data and Observation-Driven Modeling of

1198   Methane Dynamics Indicates Lower Emissions. *Journal of Geophysical Research:*

1199   *Biogeosciences*, *127*(7), e2022JG006793. https://doi.org/10.1029/2022JG006793

1200 Jung, M., Reichstein, M., Margolis, H. A., Cescatti, A., Richardson, A. D., Arain, M. A., Arneth,

1201   A., Bernhofer, C., Bonal, D., Chen, J., Gianelle, D., Gobron, N., Kiely, G., Kutsch, W.,

1202   Lasslop, G., Law, B. E., Lindroth, A., Merbold, L., Montagnani, L., … Williams, C. (2011).

1203   Global patterns of land-atmosphere fluxes of carbon dioxide, latent heat, and sensible

1204   heat derived from eddy covariance, satellite, and meteorological observations. *Journal of*

1205   *Geophysical Research: Biogeosciences*, *116*(G3).

1206   https://doi.org/10.1029/2010JG001566

1207 Jung, M., Schwalm, C., Migliavacca, M., Walther, S., Camps-Valls, G., Koirala, S., Anthoni, P.,

1208   Besnard, S., Bodesheim, P., Carvalhais, N., Chevallier, F., Gans, F., Goll, D. S., Haverd,

1209   V., Köhler, P., Ichii, K., Jain, A. K., Liu, J., Lombardozzi, D., … Reichstein, M. (2020).

1210   Scaling carbon fluxes from eddy covariance sites to globe: Synthesis and evaluation of

1211   the FLUXCOM approach. *Biogeosciences*, *17*(5), 1343–1365. https://doi.org/10.5194/bg-

1212   17-1343-2020

1213 Kim, Y., Johnson, M. S., Knox, S. H., Black, T. A., Dalmagro, H. J., Kang, M., Kim, J., &

1214   Baldocchi, D. (2020). Gap-filling approaches for eddy covariance methane fluxes: A

1215   comparison of three machine learning algorithms and a traditional method with principal

1216   component analysis. *Global Change Biology*, *26*(3), 1499–1518.

1217   https://doi.org/10.1111/gcb.14845

Kirschke, S., Bousquet, P., Ciais, P., Saunois, M., Canadell, J. G., Dlugokencky, E. J., Bergamaschi, P., Bergmann, D., Blake, D. R., Bruhwiler, L., Cameron-Smith, P., Castaldi, S., Chevallier, F., Feng, L., Fraser, A., Heimann, M., Hodson, E. L., Houweling, S., Josse, B., … Zeng, G. (2013). Three decades of global methane sources and sinks. *Nature Geoscience*, *6*(10), Article 10. https://doi.org/10.1038/ngeo1955

Knox, S. H., Bansal, S., McNicol, G., Schafer, K., Sturtevant, C., Ueyama, M., Valach, A. C., Baldocchi, D., Delwiche, K., Desai, A. R., Euskirchen, E., Liu, J., Lohila, A., Malhotra, A., Melling, L., Riley, W., Runkle, B. R. K., Turner, J., Vargas, R., … Jackson, R. B. (2021). Identifying dominant environmental predictors of freshwater wetland methane fluxes across diurnal to seasonal time scales. *Global Change Biology*, *27*(15), 3582–3604. https://doi.org/10.1111/gcb.15661

Knox, S. H., Jackson, R. B., Poulter, B., McNicol, G., Fluet-Chouinard, E., Zhang, Z., Hugelius, G., Bousquet, P., Canadell, J. G., Saunois, M., Papale, D., Chu, H., Keenan, T. F., Baldocchi, D., Torn, M. S., Mammarella, I., Trotta, C., Aurela, M., Bohrer, G., … Zona, D. (2019). FLUXNET-CH4 Synthesis Activity: Objectives, Observations, and Future Directions. *Bulletin of the American Meteorological Society*, *100*(12), 2607–2632. https://doi.org/10.1175/BAMS-D-18-0268.1

Kuhn, M. A., Varner, R. K., Bastviken, D., Crill, P., MacIntyre, S., Turetsky, M., Walter Anthony, K., McGuire, A. D., & Olefeldt, D. (2021). BAWLD-CH$_4$: A comprehensive dataset of methane fluxes from boreal and arctic ecosystems. *Earth System Science Data*, *13*(11), 5151–5189. https://doi.org/10.5194/essd-13-5151-2021

Kuter, S. (2021). Completing the machine learning saga in fractional snow cover estimation from MODIS Terra reflectance data: Random forests versus support vector regression. *Remote Sensing of Environment*, *255*, 112294. https://doi.org/10.1016/j.rse.2021.112294

Kyzivat, E. D., Smith, L. C., Garcia-Tigreros, F., Huang, C., Wang, C., Langhorst, T., Fayne, J. V., Harlan, M. E., Ishitsuka, Y., Feng, D., Dolan, W., Pitcher, L. H., Wickland, K. P., Dornblaser, M. M., Striegl, R. G., Pavelsky, T. M., Butman, D. E., & Gleason, C. J. (2022). The Importance of Lake Emergent Aquatic Vegetation for Estimating Arctic-Boreal Methane Emissions. *Journal of Geophysical Research: Biogeosciences*, *127*(6), e2021JG006635. https://doi.org/10.1029/2021JG006635

Larmola, T., Tuittila, E.-S., Tiirola, M., Nykänen, H., Martikainen, P. J., Yrjälä, K., Tuomivirta, T., & Fritze, H. (2010). The role of Sphagnum mosses in the methane cycling of a boreal mire. *Ecology*, *91*(8), 2356–2365. https://doi.org/10.1890/09-1343.1

Lehner, B., & Döll, P. (2004). Development and validation of a global database of lakes, reservoirs and wetlands. *Journal of Hydrology*, *296*(1), 1–22. https://doi.org/10.1016/j.jhydrol.2004.03.028

Lehner, B., Anand, M., Fluet-Chouinard, E., Tan, F., Aires, F., Allen, G. H., Bousquet, P., Canadell, J. G., Davidson, N., Finlayson, C. M., Gumbricht, T., Hilarides, L., Hugelius, G., Jackson, R. B., Korver, M. C., McIntyre, P. B., Nagy, S., Olefeldt, D., Pavelsky, T. M., … Thieme, M. (2024). Mapping the world’s inland surface waters: An update to the Global Lakes and Wetlands Database (GLWD v2). *Earth System Science Data Discussions*, 1–49. https://doi.org/10.5194/essd-2024-204

Li, M., Wu, P., & Ma, Z. (2020). A comprehensive evaluation of soil moisture and soil temperature from third-generation atmospheric and land reanalysis data sets. *International Journal of Climatology*, *40*(13), 5744–5766. https://doi.org/10.1002/joc.6549

Li, T., Raivonen, M., Alekseychik, P., Aurela, M., Lohila, A., Zheng, X., Zhang, Q., Wang, G., Mammarella, I., Rinne, J., Yu, L., Xie, B., Vesala, T., & Zhang, W. (2016). Importance of vegetation classes in modeling CH4 emissions from boreal and subarctic wetlands in Finland. *Science of The Total Environment*, *572*, 1111–1122. https://doi.org/10.1016/j.scitotenv.2016.08.020

Liebner, S., Zeyer, J., Wagner, D., Schubert, C., Pfeiffer, E.-M., & Knoblauch, C. (2011). Methane oxidation associated with submerged brown mosses reduces methane emissions from Siberian polygonal tundra. *Journal of Ecology*, *99*(4), 914–922. https://doi.org/10.1111/j.1365-2745.2011.01823.x

Liu, L., Xu, S., Tang, J., Guan, K., Griffis, T. J., Erickson, M. D., Frie, A. L., Jia, X., Kim, T., Miller, L. T., Peng, B., Wu, S., Yang, Y., Zhou, W., Kumar, V., & Jin, Z. (2022). KGML-ag: A modeling framework of knowledge-guided machine learning to simulate agroecosystems: a case study of estimating N_2O emission using data from mesocosm experiments. *Geoscientific Model Development*, *15*(7), 2839–2858. https://doi.org/10.5194/gmd-15-2839-2022

Ludwig, S. M., Natali, S. M., Schade, J. D., Powell, M., Fiske, G., Schiferl, L. D., & Commane, R. (2023). Scaling waterbody carbon dioxide and methane fluxes in the arctic using an integrated terrestrial-aquatic approach. *Environmental Research Letters*, *18*(6), 064019. https://doi.org/10.1088/1748-9326/acd467

Ma, H., Zeng, J., Zhang, X., Fu, P., Zheng, D., Wigneron, J.-P., Chen, N., & Niyogi, D. (2021). Evaluation of six satellite- and model-based surface soil temperature datasets using global ground-based observations. *Remote Sensing of Environment*, *264*, 112605. https://doi.org/10.1016/j.rse.2021.112605

Masson-Delmotte, V., Zhai, P., Pirani, A., Connors, S. L., Péan, C., Berger, S., Caud, N., Chen, Y., Goldfarb, L., & Gomis, M. I. (2021). Climate change 2021: The physical science basis. *Contribution of Working Group I to the Sixth Assessment Report of the Intergovernmental Panel on Climate Change*, *2*.

Mastepanov, M., Sigsgaard, C., Dlugokencky, E. J., Houweling, S., Ström, L., Tamstorf, M. P., & Christensen, T. R. (2008). Large tundra methane burst during onset of freezing. *Nature*, *456*(7222), Article 7222. https://doi.org/10.1038/nature07464

Mavrovic, A., Sonnentag, O., Lemmetyinen, J., Voigt, C., Aurela, M., & Roy, A. (2024). *Winter methane fluxes over boreal and Arctic environments*. ESS Open Archive. https://doi.org/10.22541/essoar.170542245.58670859/v1

McGuire, A. D., Anderson, L. G., Christensen, T. R., Dallimore, S., Guo, L., Hayes, D. J., Heimann, M., Lorenson, T. D., Macdonald, R. W., & Roulet, N. (2009). Sensitivity of the carbon cycle in the Arctic to climate change. *Ecological Monographs*, *79*(4), 523–555. https://doi.org/10.1890/08-2025.1

McNicol, G., Fluet-Chouinard, E., Ouyang, Z., Knox, S., Zhang, Z., Aalto, T., Bansal, S., Chang, K.-Y., Chen, M., Delwiche, K., Feron, S., Goeckede, M., Liu, J., Malhotra, A., Melton, J. R., Riley, W., Vargas, R., Yuan, K., Ying, Q., … Jackson, R. B. (2023). Upscaling Wetland Methane Emissions From the FLUXNET-CH4 Eddy Covariance Network

(UpCH4 v1.0): Model Development, Network Assessment, and Budget Comparison. *AGU Advances*, *4*(5), e2023AV000956. https://doi.org/10.1029/2023AV000956

Melack, J. M., & Hess, L. L. (2023). Areal extent of vegetative cover: A challenge to regional upscaling of methane emissions. *Aquatic Botany*, *184*, 103592. https://doi.org/10.1016/j.aquabot.2022.103592

Melton, J. R., Wania, R., Hodson, E. L., Poulter, B., Ringeval, B., Spahni, R., Bohn, T., Avis, C. A., Beerling, D. J., Chen, G., Eliseev, A. V., Denisov, S. N., Hopcroft, P. O., Lettenmaier, D. P., Riley, W. J., Singarayer, J. S., Subin, Z. M., Tian, H., Zürcher, S., … Kaplan, J. O. (2013). Present state of global wetland extent and wetland methane modelling: Conclusions from a model inter-comparison project (WETCHIMP). *Biogeosciences*, *10*(2), 753–788. https://doi.org/10.5194/bg-10-753-2013

Miller, S. M., Miller, C. E., Commane, R., Chang, R. Y.-W., Dinardo, S. J., Henderson, J. M., Karion, A., Lindaas, J., Melton, J. R., Miller, J. B., Sweeney, C., Wofsy, S. C., & Michalak, A. M. (2016). A multiyear estimate of methane fluxes in Alaska from CARVE atmospheric observations. *Global Biogeochemical Cycles*, *30*(10), 1441–1453. https://doi.org/10.1002/2016GB005419

Miner, K. R., Turetsky, M. R., Malina, E., Bartsch, A., Tamminen, J., McGuire, A. D., Fix, A., Sweeney, C., Elder, C. D., & Miller, C. E. (2022). Permafrost carbon emissions in a changing Arctic. *Nature Reviews Earth & Environment*, *3*(1), Article 1. https://doi.org/10.1038/s43017-021-00230-3

Murray-Hudson, M., Wolski, P., Cassidy, L., Brown, M. T., Thito, K., Kashe, K., & Mosimanyana, E. (2015). Remote Sensing-derived hydroperiod as a predictor of floodplain vegetation composition. *Wetlands Ecology and Management*, *23*(4), 603–616. https://doi.org/10.1007/s11273-014-9340-z

Natali, S. M., Watts, J. D., Rogers, B. M., Potter, S., Ludwig, S. M., Selbmann, A.-K., Sullivan, P. F., Abbott, B. W., Arndt, K. A., Birch, L., Björkman, M. P., Bloom, A. A., Celis, G., Christensen, T. R., Christiansen, C. T., Commane, R., Cooper, E. J., Crill, P., Czimczik, C., … Zona, D. (2019). Large loss of CO2 in winter observed across the northern permafrost region. *Nature Climate Change*, *9*(11), Article 11. https://doi.org/10.1038/s41558-019-0592-8

Olefeldt, D., Euskirchen, E. S., Harden, J., Kane, E., McGuire, A. D., Waldrop, M. P., & Turetsky, M. R. (2017). A decade of boreal rich fen greenhouse gas fluxes in response to natural and experimental water table variability. *Global Change Biology*, *23*(6), 2428–2440. https://doi.org/10.1111/gcb.13612

Olefeldt, D., Hovemyr, M., Kuhn, M. A., Bastviken, D., Bohn, T. J., Connolly, J., Crill, P., Euskirchen, E. S., Finkelstein, S. A., Genet, H., Grosse, G., Harris, L. I., Heffernan, L., Helbig, M., Hugelius, G., Hutchins, R., Juutinen, S., Lara, M. J., Malhotra, A., … Watts, J. D. (2021). The Boreal–Arctic Wetland and Lake Dataset (BAWLD). *Earth System Science Data*, *13*(11), 5127–5149. https://doi.org/10.5194/essd-13-5127-2021

Olefeldt, D., Turetsky, M. R., Crill, P. M., & McGuire, A. D. (2013). Environmental and physical controls on northern terrestrial methane emissions across permafrost zones. *Global Change Biology*, *19*(2), 589–603. https://doi.org/10.1111/gcb.12071

Osterkamp, T. E., Viereck, L., Shur, Y., Jorgenson, M. T., Racine, C., Doyle, A., & Boone, R. D. (2000). Observations of Thermokarst and Its Impact on Boreal Forests in Alaska, U.S.A.

Arctic, Antarctic, and Alpine Research, *32*(3), 303–315.
https://doi.org/10.1080/15230430.2000.12003368

Ouyang, Z., Jackson, R. B., McNicol, G., Fluet-Chouinard, E., Runkle, B. R. K., Papale, D.,
Knox, S. H., Cooley, S., Delwiche, K. B., Feron, S., Irvin, J. A., Malhotra, A., Muddasir,
M., Sabbatini, S., Alberto, Ma. C. R., Cescatti, A., Chen, C.-L., Dong, J., Fong, B. N., …
Zhang, Y. (2023). Paddy rice methane emissions across Monsoon Asia. *Remote
Sensing of Environment*, *284*, 113335. https://doi.org/10.1016/j.rse.2022.113335

Pallandt, M. M. T. A., Kumar, J., Mauritz, M., Schuur, E. A. G., Virkkala, A.-M., Celis, G.,
Hoffman, F. M., & Göckede, M. (2022). Representativeness assessment of the pan-
Arctic eddy covariance site network and optimized future enhancements.
Biogeosciences, *19*(3), 559–583. https://doi.org/10.5194/bg-19-559-2022

Pedregosa, F., Varoquaux, G., Gramfort, A., Michel, V., Thirion, B., Grisel, O., Blondel, M.,
Prettenhofer, P., Weiss, R., & Dubourg, V. (2011). Scikit-learn: Machine learning in
Python. *The Journal of Machine Learning Research*, *12*, 2825–2830.

Peltola, O., Vesala, T., Gao, Y., Räty, O., Alekseychik, P., Aurela, M., Chojnicki, B., Desai, A.
R., Dolman, A. J., Euskirchen, E. S., Friborg, T., Göckede, M., Helbig, M., Humphreys,
E., Jackson, R. B., Jocher, G., Joos, F., Klatt, J., Knox, S. H., … Aalto, T. (2019).
Monthly gridded data product of northern wetland methane emissions based on
upscaling eddy covariance observations. *Earth System Science Data*, *11*(3), 1263–1289.
https://doi.org/10.5194/essd-11-1263-2019

Peng, J., Loew, A., Merlin, O., & Verhoest, N. E. C. (2017). A review of spatial downscaling of
satellite remotely sensed soil moisture. *Reviews of Geophysics*, *55*(2), 341–366.
https://doi.org/10.1002/2016RG000543

Peng, S., Lin, X., Thompson, R. L., Xi, Y., Liu, G., Hauglustaine, D., Lan, X., Poulter, B.,
Ramonet, M., Saunois, M., Yin, Y., Zhang, Z., Zheng, B., & Ciais, P. (2022). Wetland
emission and atmospheric sink changes explain methane growth in 2020. *Nature*,
612(7940), Article 7940. https://doi.org/10.1038/s41586-022-05447-w

Prigent, C., Jimenez, C., & Bousquet, P. (2020). Satellite-Derived Global Surface Water Extent
and Dynamics Over the Last 25 Years (GIEMS-2). *Journal of Geophysical Research:
Atmospheres*, *125*(3), e2019JD030711. https://doi.org/10.1029/2019JD030711

Ramage, J., Kuhn, M., Virkkala, A.-M., Voigt, C., Marushchak, M. E., Bastos, A., Biasi, C.,
Canadell, J. G., Ciais, P., López-Blanco, E., Natali, S. M., Olefeldt, D., Potter, S.,
Poulter, B., Rogers, B. M., Schuur, E. A. G., Treat, C., Turetsky, M. R., Watts, J., &
Hugelius, G. (2024). The Net GHG Balance and Budget of the Permafrost Region
(2000–2020) From Ecosystem Flux Upscaling. *Global Biogeochemical Cycles*, *38*(4),
e2023GB007953. https://doi.org/10.1029/2023GB007953

Rawlins, M. A., Steele, M., Holland, M. M., Adam, J. C., Cherry, J. E., Francis, J. A., Groisman,
P. Y., Hinzman, L. D., Huntington, T. G., Kane, D. L., Kimball, J. S., Kwok, R., Lammers,
R. B., Lee, C. M., Lettenmaier, D. P., McDonald, K. C., Podest, E., Pundsack, J. W.,
Rudels, B., … Zhang, T. (2010). Analysis of the Arctic System for Freshwater Cycle
Intensification: Observations and Expectations. *Journal of Climate*, *23*(21), 5715–5737.
https://doi.org/10.1175/2010JCLI3421.1

Reichle, R. H., Lannoy, G. J. M. D., Liu, Q., Koster, R. D., Kimball, J. S., Crow, W. T.,
Ardizzone, J. V., Chakraborty, P., Collins, D. W., Conaty, A. L., Girotto, M., Jones, L. A.,

Kolassa, J., Lievens, H., Lucchesi, R. A., & Smith, E. B. (2017). Global Assessment of the SMAP Level-4 Surface and Root-Zone Soil Moisture Product Using Assimilation Diagnostics. *Journal of Hydrometeorology*, *18*(12), 3217–3237. https://doi.org/10.1175/JHM-D-17-0130.1

Reichstein, M., Camps-Valls, G., Stevens, B., Jung, M., Denzler, J., Carvalhais, N., & Prabhat. (2019). Deep learning and process understanding for data-driven Earth system science. *Nature*, *566*(7743), Article 7743. https://doi.org/10.1038/s41586-019-0912-1

Rocher-Ros, G., Stanley, E. H., Loken, L. C., Casson, N. J., Raymond, P. A., Liu, S., Amatulli, G., & Sponseller, R. A. (2023). Global methane emissions from rivers and streams. *Nature*, *621*(7979), Article 7979. https://doi.org/10.1038/s41586-023-06344-6

Rosentreter, J. A., Borges, A. V., Deemer, B. R., Holgerson, M. A., Liu, S., Song, C., Melack, J., Raymond, P. A., Duarte, C. M., Allen, G. H., Olefeldt, D., Poulter, B., Battin, T. I., & Eyre, B. D. (2021). Half of global methane emissions come from highly variable aquatic ecosystem sources. *Nature Geoscience*, *14*(4), Article 4. https://doi.org/10.1038/s41561-021-00715-2

Rößger, N., Sachs, T., Wille, C., Boike, J., & Kutzbach, L. (2022). Seasonal increase of methane emissions linked to warming in Siberian tundra. *Nature Climate Change*, 1–6. https://doi.org/10.1038/s41558-022-01512-4

Saikia, P., Baruah, R. D., Singh, S. K., & Chaudhuri, P. K. (2020). Artificial Neural Networks in the domain of reservoir characterization: A review from shallow to deep models. *Computers & Geosciences*, *135*, 104357. https://doi.org/10.1016/j.cageo.2019.104357

Saunois, M., Stavert, A. R., Poulter, B., Bousquet, P., Canadell, J. G., Jackson, R. B., Raymond, P. A., Dlugokencky, E. J., Houweling, S., Patra, P. K., Ciais, P., Arora, V. K., Bastviken, D., Bergamaschi, P., Blake, D. R., Brailsford, G., Bruhwiler, L., Carlson, K. M., Carrol, M., … Zhuang, Q. (2020). The Global Methane Budget 2000–2017. *Earth System Science Data*, *12*(3), 1561–1623. https://doi.org/10.5194/essd-12-1561-2020

Schaaf, C. B., Gao, F., Strahler, A. H., Lucht, W., Li, X., Tsang, T., Strugnell, N. C., Zhang, X., Jin, Y., Muller, J.-P., Lewis, P., Barnsley, M., Hobson, P., Disney, M., Roberts, G., Dunderdale, M., Doll, C., d'Entremont, R. P., Hu, B., … Roy, D. (2002). First operational BRDF, albedo nadir reflectance products from MODIS. *Remote Sensing of Environment*, *83*(1), 135–148. https://doi.org/10.1016/S0034-4257(02)00091-3

Schiferl, L. D., Watts, J. D., Larson, E. J. L., Arndt, K. A., Biraud, S. C., Euskirchen, E. S., Goodrich, J. P., Henderson, J. M., Kalhori, A., McKain, K., Mountain, M. E., Munger, J. W., Oechel, W. C., Sweeney, C., Yi, Y., Zona, D., & Commane, R. (2022). Using atmospheric observations to quantify annual biogenic carbon dioxide fluxes on the Alaska North Slope. *Biogeosciences*, *19*(24), 5953–5972. https://doi.org/10.5194/bg-19-5953-2022

Smith, S. L., O'Neill, H. B., Isaksen, K., Noetzli, J., & Romanovsky, V. E. (2022). The changing thermal state of permafrost. *Nature Reviews Earth & Environment*, *3*(1), Article 1. https://doi.org/10.1038/s43017-021-00240-1

Spahni, R., Wania, R., Neef, L., van Weele, M., Pison, I., Bousquet, P., Frankenberg, C., Foster, P. N., Joos, F., Prentice, I. C., & van Velthoven, P. (2011). Constraining global methane emissions and uptake by ecosystems. *Biogeosciences*, *8*(6), 1643–1665. https://doi.org/10.5194/bg-8-1643-2011

1437   Thornton, B. F., Wik, M., & Crill, P. M. (2016). Double-counting challenges the accuracy of high-
1438   latitude methane inventories. *Geophysical Research Letters*, *43*(24), 12,569-12,577.
1439   https://doi.org/10.1002/2016GL071772
1440   Tramontana, G., Jung, M., Schwalm, C. R., Ichii, K., Camps-Valls, G., Ráduly, B., Reichstein,
1441   M., Arain, M. A., Cescatti, A., Kiely, G., Merbold, L., Serrano-Ortiz, P., Sickert, S., Wolf,
1442   S., & Papale, D. (2016). Predicting carbon dioxide and energy fluxes across global
1443   FLUXNET sites with regression algorithms. *Biogeosciences*, *13*(14), 4291–4313.
1444   https://doi.org/10.5194/bg-13-4291-2016
1445   Treat, C. C., Bloom, A. A., & Marushchak, M. E. (2018). Nongrowing season methane
1446   emissions–a significant component of annual emissions across northern ecosystems.
1447   *Global Change Biology*, *24*(8), 3331–3343. https://doi.org/10.1111/gcb.14137
1448   Treat, C. C., Virkkala, A.-M., Burke, E., Bruhwiler, L., Chatterjee, A., Fisher, J. B., Hashemi, J.,
1449   Parmentier, F.-J. W., Rogers, B. M., Westermann, S., Watts, J. D., Blanc-Betes, E.,
1450   Fuchs, M., Kruse, S., Malhotra, A., Miner, K., Strauss, J., Armstrong, A., Epstein, H.
1451   E., … Hugelius, G. (2024). Permafrost Carbon: Progress on Understanding Stocks and
1452   Fluxes Across Northern Terrestrial Ecosystems. *Journal of Geophysical Research:*
1453   *Biogeosciences*, *129*(3), e2023JG007638. https://doi.org/10.1029/2023JG007638
1454   Turner, J., Desai, A. R., Thom, J., & Wickland, K. P. (2021). Lagged Wetland CH4 Flux
1455   Response in a Historically Wet Year. *Journal of Geophysical Research: Biogeosciences*,
1456   *126*(11), e2021JG006458. https://doi.org/10.1029/2021JG006458
1457   Ueyama, M., Iwata, H., Endo, R., & Harazono, Y. (2023). Methane and carbon dioxide
1458   emissions from the forest floor of a black spruce forest on permafrost in interior Alaska.
1459   *Polar Science*, *35*, 100921. https://doi.org/10.1016/j.polar.2022.100921
1460   Ueyama, M., Knox, S. H., Delwiche, K. B., Bansal, S., Riley, W. J., Baldocchi, D., Hirano, T.,
1461   McNicol, G., Schafer, K., Windham-Myers, L., Poulter, B., Jackson, R. B., Chang, K.-Y.,
1462   Chen, J., Chu, H., Desai, A. R., Gogo, S., Iwata, H., Kang, M., … Sachs, T. (2023).
1463   Modeled production, oxidation, and transport processes of wetland methane emissions
1464   in temperate, boreal, and Arctic regions. *Global Change Biology*, *29*(8), 2313–2334.
1465   https://doi.org/10.1111/gcb.16594
1466   Upton, S., Reichstein, M., Gans, F., Peters, W., Kraft, B., & Bastos, A. (2023). Constraining
1467   biospheric carbon dioxide fluxes by combined top-down and bottom-up approaches.
1468   *EGUsphere*, 1–31. https://doi.org/10.5194/egusphere-2023-805
1469   van Hulzen, J. B., Segers, R., van Bodegom, P. M., & Leffelaar, P. A. (1999). Temperature
1470   effects on soil methane production: An explanation for observed variability. *Soil Biology*
1471   *and Biochemistry, 31*(14), 1919–1929. https://doi.org/10.1016/S0038-0717(99)00109-1
1472   Villarreal, S., & Vargas, R. (2021). Representativeness of FLUXNET Sites Across Latin
1473   America. *Journal of Geophysical Research: Biogeosciences*, *126*(3), e2020JG006090.
1474   https://doi.org/10.1029/2020JG006090
1475   Virkkala, A.-M., Aalto, J., Rogers, B. M., Tagesson, T., Treat, C. C., Natali, S. M., Watts, J. D.,
1476   Potter, S., Lehtonen, A., Mauritz, M., Schuur, E. A. G., Kochendorfer, J., Zona, D.,
1477   Oechel, W., Kobayashi, H., Humphreys, E., Goeckede, M., Iwata, H., Lafleur, P. M., …
1478   Luoto, M. (2021). Statistical upscaling of ecosystem CO2 fluxes across the terrestrial
1479   tundra and boreal domain: Regional patterns and uncertainties. *Global Change Biology*,
1480   *27*(17), 4040–4059. https://doi.org/10.1111/gcb.15659

Virkkala, A.-M., Niittynen, P., Kemppinen, J., Marushchak, M. E., Voigt, C., Hensgens, G., Kerttula, J., Happonen, K., Tyystjärvi, V., Biasi, C., Hultman, J., Rinne, J., & Luoto, M. (2023). High-resolution spatial patterns and drivers of terrestrial ecosystem carbon dioxide, methane, and nitrous oxide fluxes in the tundra. *Biogeosciences Discussions*, 1–29. https://doi.org/10.5194/bg-2023-61

Voigt, C., Virkkala, A.-M., Hould Gosselin, G., Bennett, K. A., Black, T. A., Detto, M., Chevrier-Dion, C., Guggenberger, G., Hashmi, W., Kohl, L., Kou, D., Marquis, C., Marsh, P., Marushchak, M. E., Nesic, Z., Nykänen, H., Saarela, T., Sauheitl, L., Walker, B., … Sonnentag, O. (2023). Arctic soil methane sink increases with drier conditions and higher ecosystem respiration. *Nature Climate Change*, *13*(10), Article 10. https://doi.org/10.1038/s41558-023-01785-3

Walsh, J. E. (2014). Intensified warming of the Arctic: Causes and impacts on middle latitudes. *Global and Planetary Change*, *117*, 52–63. https://doi.org/10.1016/j.gloplacha.2014.03.003

Wang, W., Rinke, A., Moore, J. C., Ji, D., Cui, X., Peng, S., Lawrence, D. M., McGuire, A. D., Burke, E. J., Chen, X., Decharme, B., Koven, C., MacDougall, A., Saito, K., Zhang, W., Alkama, R., Bohn, T. J., Ciais, P., Delire, C., … Sherstiukov, A. B. (2016). Evaluation of air–soil temperature relationships simulated by land surface models during winter across the permafrost region. *The Cryosphere*, *10*(4), 1721–1737. https://doi.org/10.5194/tc-10-1721-2016

Wang, Z., Schaaf, C. B., Sun, Q., Shuai, Y., & Román, M. O. (2018). Capturing rapid land surface dynamics with Collection V006 MODIS BRDF/NBAR/Albedo (MCD43) products. *Remote Sensing of Environment*, *207*, 50–64. https://doi.org/10.1016/j.rse.2018.02.001

Watts, J. D., Farina, M., Kimball, J. S., Schiferl, L. D., Liu, Z., Arndt, K. A., Zona, D., Ballantyne, A., Euskirchen, E. S., Parmentier, F.-J. W., Helbig, M., Sonnentag, O., Tagesson, T., Rinne, J., Ikawa, H., Ueyama, M., Kobayashi, H., Sachs, T., Nadeau, D. F., … Oechel, W. C. (2023). Carbon uptake in Eurasian boreal forests dominates the high-latitude net ecosystem carbon budget. *Global Change Biology*, *29*(7), 1870–1889. https://doi.org/10.1111/gcb.16553

Watts, J. D., Kimball, J. S., Parmentier, F. J. W., Sachs, T., Rinne, J., Zona, D., Oechel, W., Tagesson, T., Jackowicz-Korczyński, M., & Aurela, M. (2014). A satellite data driven biophysical modeling approach for estimating northern peatland and tundra CO_2 and CH_4 fluxes. *Biogeosciences*, *11*(7), 1961–1980. https://doi.org/10.5194/bg-11-1961-2014

Wik, M., Varner, R. K., Anthony, K. W., MacIntyre, S., & Bastviken, D. (2016). Climate-sensitive northern lakes and ponds are critical components of methane release. *Nature Geoscience*, *9*(2), Article 2. https://doi.org/10.1038/ngeo2578

Wrona, E., Rowlandson, T. L., Nambiar, M., Berg, A. A., Colliander, A., & Marsh, P. (2017). Validation of the Soil Moisture Active Passive (SMAP) satellite soil moisture retrieval in an Arctic tundra environment. *Geophysical Research Letters*, *44*(9), 4152–4158. https://doi.org/10.1002/2017GL072946

Yamazaki, D., Ikeshima, D., Tawatari, R., Yamaguchi, T., O'Loughlin, F., Neal, J. C., Sampson, C. C., Kanae, S., & Bates, P. D. (2017). A high-accuracy map of global terrain

elevations. *Geophysical Research Letters*, *44*(11), 5844–5853. https://doi.org/10.1002/2017GL072874

Yuan, K., Li, F., McNicol, G., Chen, M., Hoyt, A., Knox, S., Riley, W. J., Jackson, R., & Zhu, Q. (2024). Boreal–Arctic wetland methane emissions modulated by warming and vegetation activity. *Nature Climate Change*, 1–7. https://doi.org/10.1038/s41558-024-01933-3

Yuan, K., Zhu, Q., Li, F., Riley, W. J., Torn, M., Chu, H., McNicol, G., Chen, M., Knox, S., Delwiche, K., Wu, H., Baldocchi, D., Ma, H., Desai, A. R., Chen, J., Sachs, T., Ueyama, M., Sonnentag, O., Helbig, M., … Jackson, R. (2022). Causality guided machine learning model on wetland CH4 emissions across global wetlands. *Agricultural and Forest Meteorology*, *324*, 109115. https://doi.org/10.1016/j.agrformet.2022.109115

Zhang, C., Comas, X., & Brodylo, D. (2020). A Remote Sensing Technique to Upscale Methane Emission Flux in a Subtropical Peatland. *Journal of Geophysical Research: Biogeosciences*, *125*(10), e2020JG006002. https://doi.org/10.1029/2020JG006002

Zhang, Z., Bansal, S., Chang, K.-Y., Fluet-Chouinard, E., Delwiche, K., Goeckede, M., Gustafson, A., Knox, S., Leppänen, A., Liu, L., Liu, J., Malhotra, A., Markkanen, T., McNicol, G., Melton, J. R., Miller, P. A., Peng, C., Raivonen, M., Riley, W. J., … Poulter, B. (2023). Characterizing Performance of Freshwater Wetland Methane Models Across Time Scales at FLUXNET-CH4 Sites Using Wavelet Analyses. *Journal of Geophysical Research: Biogeosciences*, *128*(11), e2022JG007259. https://doi.org/10.1029/2022JG007259

Zhang, Z., Fluet-Chouinard, E., Jensen, K., McDonald, K., Hugelius, G., Gumbricht, T., Carroll, M., Prigent, C., Bartsch, A., & Poulter, B. (2021). Development of the global dataset of Wetland Area and Dynamics for Methane Modeling (WAD2M). *Earth System Science Data*, *13*(5), 2001–2023. https://doi.org/10.5194/essd-13-2001-2021

Zhang, Z., Poulter, B., Feldman, A. F., Ying, Q., Ciais, P., Peng, S., & Li, X. (2023). Recent intensification of wetland methane feedback. *Nature Climate Change*, *13*(5), Article 5. https://doi.org/10.1038/s41558-023-01629-0

Zona, D., Gioli, B., Commane, R., Lindaas, J., Wofsy, S. C., Miller, C. E., Dinardo, S. J., Dengel, S., Sweeney, C., Karion, A., Chang, R. Y.-W., Henderson, J. M., Murphy, P. C., Goodrich, J. P., Moreaux, V., Liljedahl, A., Watts, J. D., Kimball, J. S., Lipson, D. A., & Oechel, W. C. (2016). Cold season emissions dominate the Arctic tundra methane budget. *Proceedings of the National Academy of Sciences*, *113*(1), 40–45. https://doi.org/10.1073/pnas.1516017113